

GridFormer: Residual Dense Transformer with Grid Structure for Image Restoration in Adverse Weather Conditions

Tao Wang · Kaihao Zhang · Ziqian Shao · Wenhan Luo ·
Bjorn Stenger · Tong Lu · Tae-Kyun Kim · Wei Liu · Hongdong Li

Received: date / Accepted: date

Abstract Image restoration in adverse weather conditions is a difficult task in computer vision. In this paper, we propose a novel transformer-based framework called GridFormer which serves as a backbone for image restoration under adverse weather conditions. GridFormer is designed in a grid structure using a residual dense transformer block, and it introduces two core designs. First, it uses an enhanced attention mechanism

in the transformer layer. The mechanism includes stages of the sampler and compact self-attention to improve efficiency, and a local enhancement stage to strengthen local information. Second, we introduce a residual dense transformer block (RDTB) as the final GridFormer layer. This design further improves the network’s ability to learn effective features from both preceding and current local features. The GridFormer framework achieves state-of-the-art results on five diverse image restoration tasks in adverse weather conditions, including image deraining, dehazing, deraining & dehazing, desnowing, and multi-weather restoration. The source code and pre-trained models are available at <https://github.com/TaoWangzj/GridFormer>.

Tao Wang, Ziqian Shao and Tong Lu
Nanjing University, Nanjing, 210023, China
E-mail: taowangzj@gmail.com, ziqian.shao@outlook.com, lutong@nju.edu.cn

Kaihao Zhang
Harbin Institute of Technology, Shenzhen, 518055, China
E-mail: super.khzhang@gmail.com

Wenhan Luo
Hong Kong University of Science and Technology, Hong Kong
E-mail: whluo.china@gmail.com

Bjorn Stenger
Rakuten Institute of Technology, Japan
E-mail: bjorn@cantab.net

Tae-Kyun Kim
Imperial College London, London, UK & KAIST, Daejeon, South Korea
E-mail: tk.kim@imperial.ac.uk

Wei Liu
Tencent, Shenzhen, 518107, China
E-mail: wl2223@columbia.edu

Hongdong Li
Australian National University, Australia
E-mail: hongdong.li@gmail.com

1 Introduction

Capturing high-quality images in adverse weather conditions like rain, haze, and snow is a challenging task due to the complex degradation that occurs in such conditions. These include color distortion, blur, noise, low contrast, and other issues that directly lower the visual quality. Furthermore, such degradation can lead to difficulties in downstream computer vision tasks such as object recognition and scene understanding [26, 6].

Traditional methods for image restoration in adverse weather conditions often rely on handcrafted priors such as smoothness and dark channel, with linear transformations [65, 19, 22, 12]. However, these methods are limited in their ability to address complex weather conditions due to poor prior generalization. Recently, convolutional neural network (CNN) based methods have been proposed to handle the problems of image deraining [18, 75, 88], dehazing [4, 62, 94], and desnowing [49, 39, 97]. These methods focus on learning

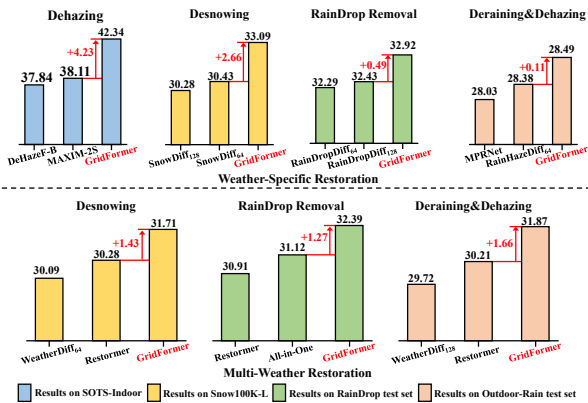


Fig. 1 Comparison results for image restoration in adverse weather conditions. Results on (top) weather-specific restoration, and (bottom) multi-weather restoration tasks, showing state-of-the-art performance in terms of PSNR.

a mapping from the weather-degraded image to the restored image using specific architectural designs, such as residual learning [47, 29], multi-scale or multi-stage networks [14, 97], dense connections [46, 97], GAN structure [59, 27], and attention mechanism [99, 92]. However, these methods are often designed for a single specific task and may not work well for multi-weather restoration.

Recently, a new approach has emerged to address the challenge of multi-weather restoration in a unified architecture [41, 71, 35, 54]. The pioneering work of Li *et al.* [41] proposes a multi-encoder and decoder network, with each encoder dedicated to processing one type of degradation. The network is optimized using neural architecture search. Subsequent works have borrowed this structure to improve multi-weather restoration performance. For instance, Valanarasu *et al.* [71] introduced the TransWeather network that employs self-attention for multi-weather restoration. Although TransWeather is more efficient than the task-specific encoder network, its performance is constrained by its inadequate exploitation of feature fusion across different scales in the network. Recently, some works focus on designing the general backbone network to exploit multi-scale features in the network for vision tasks. For example, HRNet [74] and HRFormer [90] are built by multi-resolution parallel design to learn high-resolution representations. RevCo [5] adopts the design of using columns (each column is a subnetwork), which aims to learn disentangled representations. These methods work well on human pose estimation, semantic segmentation, object detection, *etc.* However, there are currently no specifically designed transformer-based methods to effectively utilize these features to recover degraded images under severe weather conditions.

In this paper, we propose GridFormer, a transformer-based network for image restoration in adverse weather conditions. GridFormer uses residual dense transformer blocks (RDTB) embedded in a grid structure to exploit hierarchical image features. The RDTB, as the key unit of the GridFormer, contains compact-enhanced transformer layers with dense connections, and local feature fusion with local skip connections. The compact-enhanced transformer layer employs a sampler and compact self-attention for efficiency and a local enhancement stage for strengthening local details. We evaluate GridFormer on weather degradation benchmarks, including RainDrop [56], SOTS-indoor [37], Haze4K [48], Outdoor-Rain [40], and Snow100K [49], see Fig. 1.

In summary, the contributions of this work are three-fold:

- **Unified Framework:** We propose a novel and unified framework called GridFormer, which is tailored specifically for image restoration under adverse weather conditions. This innovative framework seamlessly integrates residual dense transformer blocks (RDTBs) with a grid structure, creating a comprehensive architecture. Notably, incorporating RDTBs within a grid structure enables GridFormer to capture hierarchical image features efficiently. The grid structure facilitates the integration of contextual information from various spatial scales, enhancing the network’s ability to restore images effectively.
- **Compact-enhanced Self-Attention:** GridFormer introduces the compact-enhanced self-attention mechanism, a critical contribution. This mechanism enhances the local modeling capacity of transformer units, enabling GridFormer to capture fine-grained details in adverse weather conditions while improving network efficiency.
- **State-of-the-art Performance:** We show the general applicability of our GridFormer by applying it to five diverse image restoration tasks in adverse weather conditions, including image deraining, image dehazing, image deraining & dehazing, desnowing, and multi-weather restoration. Our GridFormer achieves a new state-of-the-art on both weather-specific and multi-weather restoration tasks.

The remainder of this paper is organized as follows: Sec. 2 discusses the related work. Sec. 3 introduces our proposed method. Then, experimental results are reported and analyzed in Sec. 4. Sec. 5 discusses limitations and future work. Finally, Sec. 6 presents a conclusion of this paper.

2 Related Work

The proposed method is related to image restoration in adverse weather conditions and transformer architecture, which are reviewed in the following.

2.1 Restoration in Adverse Weather Conditions

Image restoration in adverse weather conditions is the task of restoring a high-quality image under weather-related foreground degradations like rain, fog, and snow. Especially, image restoration in adverse weather conditions typically includes image deraining [2, 32, 40, 82, 73], image dehazing [3, 4, 63, 46], image desnowing [64, 49, 97], and multi-weather restoration [41, 71, 54]. The traditional model-based methods [22, 52, 104] focus on exploring appropriate weather-related priors to address the image restoration problem. However, there has been a surge in the number of data-driven methods proposed in recent years. Next, we mainly discuss these data-driven methods in detail.

Deraining: The task of removing rain streaks from images has been approached using a deep network called DerainNet, proposed by Fu *et al.* [18]. This approach learns the nonlinear mapping between clean and rainy detail layers. Several techniques have been proposed to improve performance, such as the recurrent context aggregation in RESCAN [43], spatial attention in SPANet [75], multi-stream dense architecture in DID-MDN [95], conditional GAN-based method in [96], and conditional variational deraining based on VAEs [17]. Another approach to image deraining is removing raindrops. Yamashita *et al.* [81] developed a stereo system to detect and remove raindrops, while You *et al.* [88] proposed a motion-based method. Qian *et al.* [56] developed a raindrop removal benchmark and proposed an attentive GAN. Quan *et al.* [61] introduced an image-to-image CNN embedded attention mechanism to recover rain-free images, and Liu *et al.* [47] designed a dual residual network to remove raindrops. Zhang *et al.* [101] proposed a multifocal attention-based cross-scale network that employs spatial and channel attention to explore cross-scale correlations of rain streaks and background for image draining. Recent works aim to remove both streaks and raindrops from images simultaneously [60, 80].

Dehazing: Two pioneering methods for image dehazing are DehazeNet [4] and MSCNN [62], which first estimate the transmission map and generate haze-free images using an atmosphere scattering model [53]. AOD-Net [36] represents another advancement, which estimates one variable from the transmission map

and atmospheric light. DCPDN [94] employs two sub-networks to estimate the transmission map and the atmospheric light, respectively. Recent works have focused on directly restoring clear images from hazy images, using attention mechanisms [58, 99], multi-scale structures [14, 46], GAN structures [59] and transformers [68]. The network in [46] is a similar method to our GridFormer. However, GridFormer significantly differs from [46] in several ways. First, GridFormer is the first transformer-based method for image restoration in adverse weather conditions, whereas [46] is a CNN-based method specifically designed for image dehazing. GridFormer is more general in terms of its utility. Second, in each GridFormer layer, we design a novel compact-enhanced transformer layer and integrate it in a residual dense manner. This promotes feature reuse and consequently enhances feature representation, whereas [46] uses existing residual dense blocks in its network. Finally, extensive experiments demonstrate the superior performance of GridFormer compared to the method in [46].

Desnowing: In DesnowNet [49], translucency and residual generation modules were employed to restore image details. Li *et al.* [39] proposed a stacked dense network with a multi-scale structure. Chen *et al.* [11] introduced a desnowing method called JS-TASR, which is specifically developed for size- and transparency-aware snow removal. They used a joint scale and transparency-aware adversarial loss to improve the quality of the desnowed images. Li *et al.* [41] adopted the network architecture search technique to obtain excellent results. Zhang *et al.* [97] proposed a dense multi-scale desnowing network that incorporates learned semantic and geometric priors. More recently, some works [10, 98] have explored the transformer architecture and further improved the performance.

Multi-weather restoration: Beyond the above task-specific image restoration methods, recent works [41, 71, 35] attempt to address multi-weather restoration in a single architecture. Li *et al.* [41] proposed All-in-One networks with a multi-encoder and decoder structure to restore adverse multi-weather degraded images. Specifically, they adopt separate encoders for different weather degradations and resort to neural architecture search to seek the best task-specific encoder. In [35], All-in-one restoration network consists of a contrastive degraded encoder and a degradation-guided restoration network. Valanarasu *et al.* [71] proposed an end-to-end multi-weather image restoration model named TransWeather that achieves high performance on multi-weather restoration. The core insights in TransWeather are the intra-path transformer block and transformer decoder with

learnable weather-type embeddings. In this paper, our work aligns with this direction and focuses on designing a general model to address the multi-weather restoration problem. In addition, there are methods aimed at designing effective network architecture for image restoration. For example, MPRNet [92] and MAXIM [70] are general image restoration methods that have also been successful in addressing a range of adverse weather conditions. MIMOUNet [13] adopts an encoder-decoder-based U-shaped network with multi-input and multi-output to achieve image deblurring. In our method, we employ the coarse-to-fine strategy to the transformer network in the grid structure for image restoration under adverse weather conditions.

2.2 Vision Transformers in Image Restoration

Recently, vision transformers have witnessed great success in low-level image restoration. Specifically, inspired by the seminal work in [72], Chen *et al.* [9] proposed an Image Processing Transformer (IPT) for general image restoration, which employs a special multi-head and multi-tail structure to adapt for the specific image restoration tasks. However, IPT requires costly pre-training on large-scale datasets. Further, SwinIR [44] and Uformer [78] modify the original Swin Transformer block and obtain good performance with relatively low computational cost. In particular, SwinIR stacks the proposed residual transformer blocks to extract deep features for image reconstruction. Uformer adopts a U-shape structure, embedding the proposed LeWin transformer blocks to predict residual images. Yao *et al.* [84] adopted the LeWin transformer block as a basic unit and introduced the dense residual skip connection to propose a dense residual skip-connection network based on transformer called DenSformer for image denoising. Liang *et al.* [45] proposed a recursive transformer, which first introduces a recursive local window-based self-attention structure in the network. A recent method, Restormer [91], which is a multi-scale hierarchical transformer architecture, has also yielded fine restoration performance on image restoration *e.g.*, de-raining. Inspired by the success of these methods, we propose a general grid framework with novel transformer blocks to restore images in adverse weather conditions. SwinIR and DenSformer are similar methods to our GridFormer. However, while SwinIR fuses Swin Transformer and convolutional layers in its residual Swin Transformer block, our GridFormer’s residual dense block more effectively enhances feature reuse. Unlike DenSformer’s dense residual transformer block, our approach is characterized by the unique compact-enhanced self-attention mechanism, local feature fu-

sion, and local skip connections within the residual dense transformer block.

3 Method

To explore the potential use of the transformer on image restoration in adverse weather conditions for obtaining better results, we propose the GridFormer by embedding residual dense transformer blocks in a grid structure. The motivation and overall architecture of the proposed GridFormer will firstly be introduced in Sec. 3.1, and then the core component (*i.e.*, residual dense transformer block) of our GridFormer will be discussed in Sec. 3.2. Finally, the loss functions will be presented in Sec. 3.3.

3.1 Motivation and Architecture

Motivation. Our motivation arises from the urgent need for techniques that restore images captured in unfavorable weather conditions. Weather-related factors, such as haze, rain, and snow, significantly impact the quality and perception of images, which in turn affects various practical applications such as surveillance, autonomous driving, and outdoor photography. The main objective of developing the proposed GridFormer is to address the persistent challenges caused by adverse weather conditions on image quality. Our goal is to create an image restoration framework that effectively handles a range of adverse weather scenarios, thereby enhancing the quality of images affected by these conditions.

Architecture. As shown in Fig. 2, GridFormer contains three paths from the weather-degraded images to the recovered ones, where each path conducts restoration at different image resolutions. In GridFormer, the higher resolution path continuously interacts dynamically with the lower resolution path in the network to remove weather degradation accurately, and the lower resolution path provides useful global information owing to larger receptive fields. Each path is composed of seven GridFormer layers. Different paths are interlinked with a down-sampling layer, an up-sampling layer, and weighted attention fusion units to compose the columns of the GridFormer. Thanks to the grid structure with three rows and seven columns, information from different resolutions can be shared effectively. Specifically, GridFormer consists of three parts: grid head (GH), grid fusion module (GFM), and grid tail (GT). We present the details of each part in the following.

Grid head. To extract initial multi-resolution features, we use a grid head architecture to process pyra-

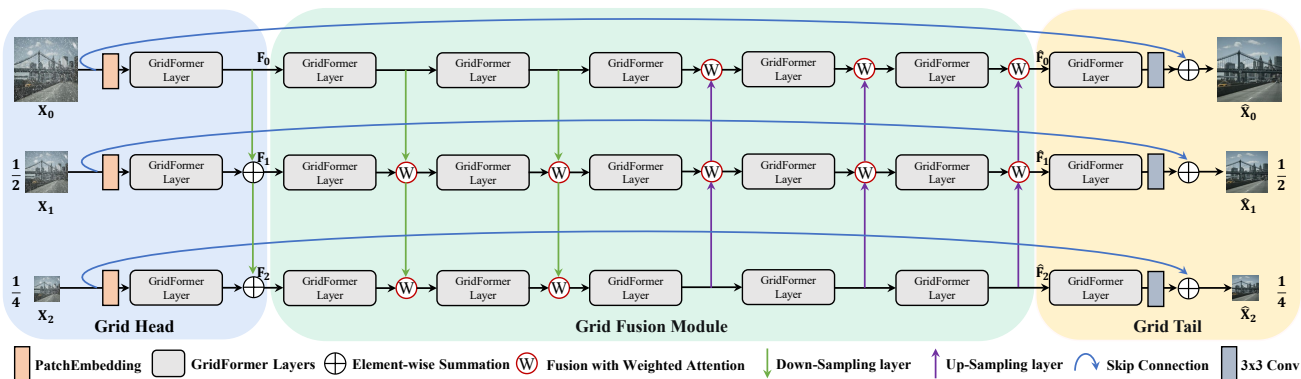


Fig. 2 GridFormer architecture. It consists of a grid head, a grid fusion module, and a grid tail. The pyramid degraded images $\mathbf{X}_0, \mathbf{X}_1, \mathbf{X}_2$ are first fed into the grid head to extract hierarchical initial features $\mathbf{F}_0, \mathbf{F}_1, \mathbf{F}_2$. The initial features are further refined by the grid fusion module to generate features $\hat{\mathbf{F}}_0, \hat{\mathbf{F}}_1, \hat{\mathbf{F}}_2$. Finally, the grid tail reconstructs clear images $\hat{\mathbf{X}}_0, \hat{\mathbf{X}}_1, \hat{\mathbf{X}}_2$.

mid input images in parallel. Every path in the grid head consists of a feature embedding layer, achieved by 3×3 convolutions, and a GridFormer layer. As shown in Fig. 2, given a weather-degraded image \mathbf{X}_0 , the grid head extracts hierarchical features $\mathbf{F} = \{\mathbf{F}_0, \mathbf{F}_1, \mathbf{F}_2\}$ in different channels (*i.e.*, C , $2C$, and $4C$) from pyramid images $\mathbf{X} = \{\mathbf{X}_0, \mathbf{X}_1, \mathbf{X}_2\}$ ($1/2$, $1/4$ scales for \mathbf{X}_1 and \mathbf{X}_2). In our experiments, we use $C = 48$. The grid head computation can be defined as:

$$\mathbf{F}_i = \begin{cases} \text{GFL}_i(\text{E}_i(\mathbf{X}_0)), & i = 0 \\ \text{GFL}_i(\text{E}_i(\mathbf{X}_i)) + (\mathbf{F}_{i-1})_{\downarrow}, & i = 1, 2 \end{cases} \quad (1)$$

where i is the i -th network path, and E_i is the feature embedding layer. The \downarrow symbol denotes the down-sampling layer, where we use a 3×3 convolution with a pixel-unshuffle operation [66] to halve the features in the spatial dimensions while doubling the channels. GFL is a GridFormer layer that is mainly built from residual dense transformer blocks.

Grid fusion module. To fully integrate the hierarchical features of different rows and columns in the network, we propose a grid fusion module between the grid head and the grid tail. The structure of the proposed grid fusion module is organized into a 2D grid pattern. As illustrated in Fig. 2, the fusion module is designed in a grid-like structure of three rows and five columns. In particular, each row contains five consecutive GridFormer layers that keep the feature dimension constant. In the column axis, according to the position in the grid, we resort to the down-sampling layers or up-sampling layers to change the size of the feature maps for feature fusion. Fig. 3 (a) shows a representative grid unit in the fusion module. The GridFormer layer is a dense structure consisting of three residual dense transformer layers (RDTL) and a 1×1 convolution, which will be discussed in the next subsection. The down-sampling and up-sampling layers are symmetrical and use a 3×3

convolution with pixel-shuffle or pixel-unshuffle operation [66] to change the feature dimensions. In addition, considering that the features of different scales may not be equally important, we use a simple weighted attention fusion strategy to achieve feature fusion from the different row and column dimensions. Inspired by [102, 76], we first generate two trainable weights for different features, where each parameter is an n -dimensional vector (n is the channels of feature). We add these weighted features to derive the fusion features. Grid units in the grid fusion module provide different information flows for feature fusion shown in Fig. 3 (b), which guides the network to produce better-recovered results in combination with different complementary information.

Grid tail. To further improve the quality of the recovered images, we design a grid tail module to predict multi-scale outputs. The structure of the grid tail is symmetrical to that of the grid head. Specifically, each path is composed of a GridFormer layer, a 3×3 convolution, and a long skip connection for image reconstruction. The skip connection is used to transmit input information directly to the grid tail module, which maintains the color and detail of the original image. The complete process is formulated as:

$$\hat{\mathbf{X}}_i = C_i(\text{GFL}_i(\hat{\mathbf{F}}_i)) + \mathbf{X}_i, i \in \{0, 1, 2\}, \quad (2)$$

where $\hat{\mathbf{X}}_i$ is the final result of GridFormer on the i -th path, C_i is a 3×3 convolution, and $\hat{\mathbf{F}}_i, i \in \{0, 1, 2\}$ is the output feature of the grid fusion module. To optimize the network parameters, we train GridFormer using a combination of two losses, multi-scale Charbonnier loss [7] and perceptual loss, where the weight of perceptual loss [31] is set to 0.1. Next, we detail the core component residual dense transformer block that is used to build the elemental layer of GridFormer.

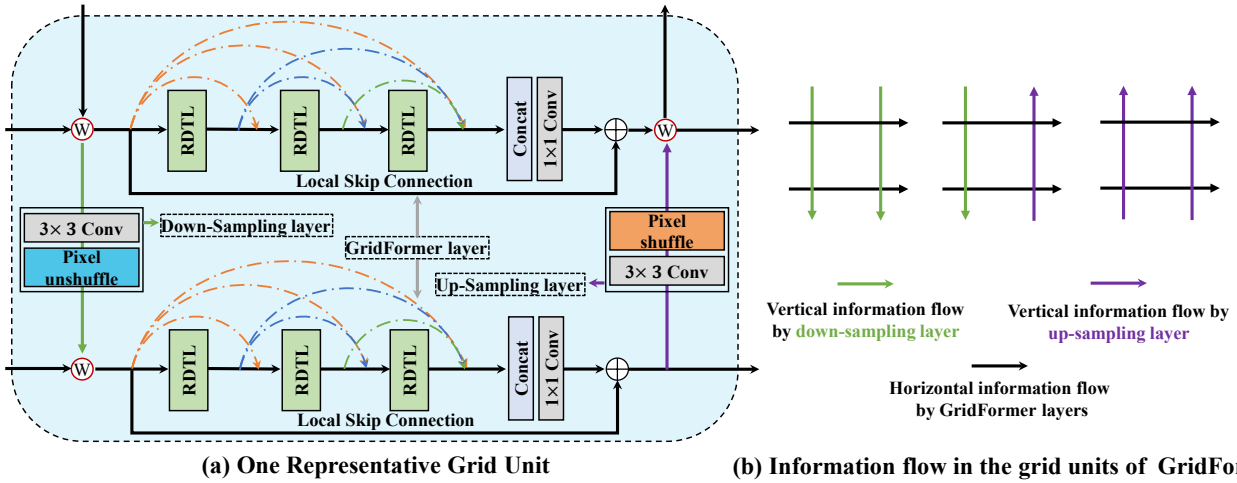


Fig. 3 Grid unit structure and information flow. (a) The structure of a single grid unit is comprised of four parts: the down-sampling layer, the GridFormer layer, the up-sampling layer, and attention fusion operations. RDTL refers to the proposed residual dense transformer layer. (b) Information flow of grid units in the fusion module.

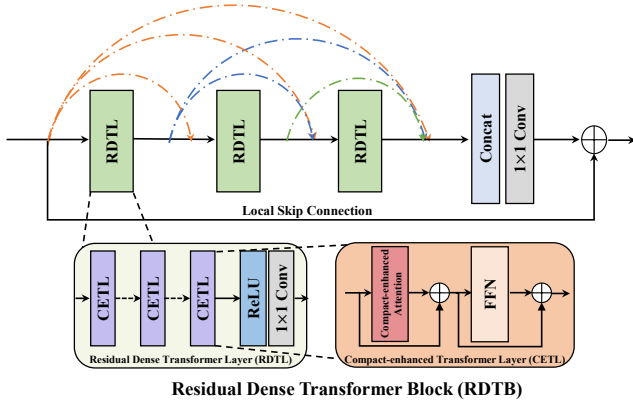


Fig. 4 The structure of the proposed Residual Dense Transformer Block (RDTB). It includes three residual dense transformer layers, a 1×1 convolution for local feature fusion, and a local skip connection for local residual learning. The residual dense transformer layer is mainly built by the proposed compact-enhance transformer layer, which contains the compact-enhanced self-attention and FFN.

3.2 Residual Dense Transformer Block

Previous works [24, 100, 46, 97, 102] have shown that using dense connections has many advantages, mitigating the vanishing gradient problem, encouraging feature reuse and enhancing information propagation. Accordingly, we propose to design the transformer with dense connections to build the basic GridFormer layers. Specifically, we propose residual dense transformer blocks (RDTB) to compose GridFormer using different settings. As illustrated in Fig. 4, RDTB contains densely connected transformer layers, local feature fusion, and local residual learning. When implementing

the dense connection, we mainly incorporate three layers of residual dense transformer layers (RDTL), with the growth rate set at 16. This implies that each individual RDTL generates 16 new feature maps. These newly generated feature maps are subsequently concatenated with the feature maps received from the preceding layer. Within each RDTL, we use several compact-enhanced transformer layers (CETL) with a ReLU [20] activation function to extract features, and adopt a 1×1 convolution to ensure the same number of channels for input and output features. For local feature fusion and local residual learning, we introduce a 1×1 convolution and a local skip connection in RDTB to control the final output.

The direct application of transformers [72, 16] to our grid network will lead to high computational overhead, we thus develop a cost-effective compact-enhanced attention, with the stages of sampler and compact self-attention for improving the efficiency, as well as a local enhancement stage for enhancing the local information in the transformer. Fig. 5 illustrates the detailed structure of the proposed compact-enhanced attention.

Feature sampling. We first design a sampler to produce down-sampled input tokens for the subsequent self-attention computation. The sampler is built by an average pooling layer with stride r . The sampler layer not only increases the receptive field to observe more information, but also enhances the invariance on the input token. In addition, the produced lower-resolution features can reduce the computation of subsequent layers. The feature sampling step is formulated as:

$$\mathbf{Z} = \text{Avg}_r(\mathbf{Z}_{in}), \quad (3)$$

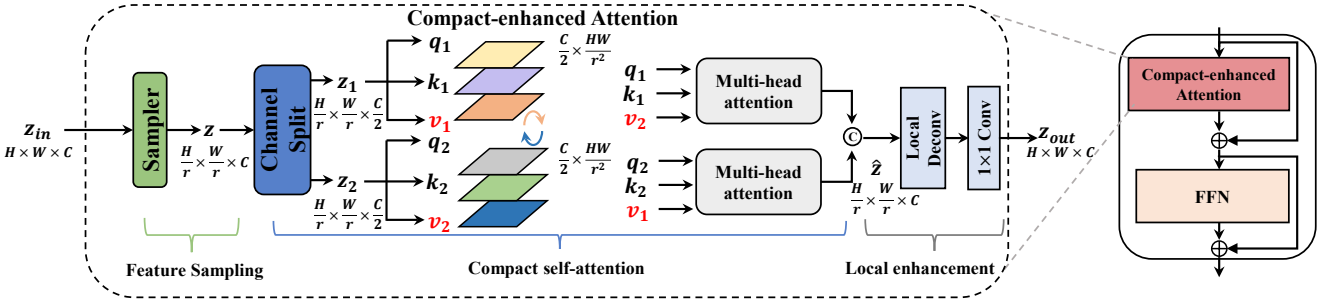


Fig. 5 **Right:** the schematic illustration of the proposed Compact-enhanced Transformer Layer consisting of a compact-enhanced attention and a Feed-Forward Network (FFN). **Left:** the compact-enhanced attention layer, which contains three steps, feature sampling, compact self-attention, and local enhancement. H , W , and C denote the height, width, and numbers of feature channels, respectively. r is the feature sampling rate. \odot and \oplus refer to concatenate and element-wise summation operations respectively.

where $\mathbf{Z}_{in} \in \mathbb{R}^{H \times W \times C}$ represents the input token. $\mathbf{Z} \in \mathbb{R}^{\frac{H}{r} \times \frac{W}{r} \times C}$ is the output token. Avg_r indicates the average pooling operation with stride r . In the experiments, we empirically set r as 4, 2, and 2 in three rows of GridFormer layers, respectively (see Sec. 4.4).

Compact self-attention. Given a feature of dimensions $H \times W \times C$, recent low-level transformer-based methods [71, 34, 78] aim to explore the long-range dependence between key and query to calculate the $N \times N$ attention map ($N = H \times W$), which leads to high complexity and fails to model the global information from the channel dimension. Thus, for more efficient computation in self-attention, we resort to a different strategy. Specifically, as illustrated in Fig. 5, for an output feature $\mathbf{Z} \in \mathbb{R}^{\frac{H}{r} \times \frac{W}{r} \times C}$ from the sampler, we first implement the split operation by dividing it along the channel dimension to produce $\mathbf{z}_1 \in \mathbb{R}^{\frac{H}{r} \times \frac{W}{r} \times \frac{C}{2}}$ and $\mathbf{z}_2 \in \mathbb{R}^{\frac{H}{r} \times \frac{W}{r} \times \frac{C}{2}}$. We then apply a convolution layer with reshape operation on \mathbf{z}_1 and \mathbf{z}_2 , which projects \mathbf{z}_1 and \mathbf{z}_2 into Queries ($\mathbf{q}_1, \mathbf{q}_2 \in \mathbb{R}^{\frac{C}{2} \times \frac{HW}{r^2}}$), Keys ($\mathbf{k}_1, \mathbf{k}_2 \in \mathbb{R}^{\frac{C}{2} \times \frac{HW}{r^2}}$) and Values ($\mathbf{v}_1, \mathbf{v}_2 \in \mathbb{R}^{\frac{C}{2} \times \frac{HW}{r^2}}$), respectively. Inspired by existing methods [55, 69, 21, 93], we exchange the values produced by them to perform multi-head self-attention, which can improve the interaction between \mathbf{z}_1 and \mathbf{z}_2 . Compared with the method of exchanging queries for feature interaction in cross-attention [55, 93], our approach exchanges the values for interaction and feature fusion, finding it beneficial for better restoration performance (see Sec. 4.4). Finally, we obtain the result $\hat{\mathbf{Z}}$ by concatenating the output of the two multi-head self-attention and changing their dimensions. The proposed compact self-attention mechanism can be formulated as:

$$\hat{\mathbf{Z}} = [\text{softmax}_1 \left(\frac{\mathbf{q}_1 \mathbf{k}_1^\top}{\sqrt{d_{k_1}}} \right) \mathbf{v}_2, \text{softmax}_2 \left(\frac{\mathbf{q}_2 \mathbf{k}_2^\top}{\sqrt{d_{k_2}}} \right) \mathbf{v}_1], \quad (4)$$

where $[\cdot]$ indicates the concatenation operation. The major computational overhead in transformers mainly

arises from the self-attention (SA) layer. In contrast to recent transformer-based methods that employ spatial modeling for SA, the complexity of the key-query dot-product interaction grows quadratically with the spatial resolution of input, *i.e.*, $O(N \times N)$. Our proposed compact self-attention addresses this by performing SA across channels instead of the spatial dimension, resulting in cross-covariance computation across channels to produce an attention map that implicitly encodes the global context. Consequently, our compact self-attention generates an attention map of size $\mathbb{R}^{C \times C}$, instead of the huge regular attention map of size $\mathbb{R}^{N \times N}$. Thus, our compact self-attention successfully reduces complexity.

Local enhancement. As shown in Fig. 5, we add a local feature enhancement stage in the tail of compact self-attention. This stage consists of a deconvolution operation, sometimes referred to as a “transposed convolution,” with a deconvolution for local feature propagation and a 1×1 convolution for local fusion:

$$\mathbf{Z}_{out} = \text{Conv}_{1 \times 1}(\text{Deconv}(\hat{\mathbf{Z}})), \quad (5)$$

where \mathbf{Z}_{out} is the final output. $\text{Conv}_{1 \times 1}$ and Deconv are 1×1 convolution and deconvolution layers respectively.

3.3 Loss Function

Inspired by existing works [87, 71, 86, 28, 42, 89, 1, 23, 57], we use a loss function combining the Charbonnier loss [7] and the perceptual loss [77] to train our GridFormer. We regard the Charbonnier loss as a pixel-wise loss, which is used between the recovered images and the ground truth images at each scale, and the perceptual loss is used to help our model produce visually pleasing results. The Charbonnier loss is defined as:

$$\mathcal{L}_{\text{char}} = \frac{1}{3} \sum_{k=0}^2 \sqrt{\|\hat{\mathbf{X}}_k - \mathbf{I}_k\|^2 + \varepsilon^2}, \quad (6)$$

where $\hat{\mathbf{X}}_k$ and \mathbf{I}_k refer to the restored image and ground-truth image respectively, and k represents the index of the image scale level in our GridFormer. The constant ε is empirically set to 10^{-3} . For the perceptual loss, following previous work [77], we adopt a pre-trained VGG19 [67] to extract the perceptual features from the *Conv5.4* layer of VGG19, and then use the L_1 loss function to compute the difference between the perceptual features of the restored images and their corresponding ground truths. This effective perceptual loss focuses on capturing high-level semantic information, resulting in sharper edges and visually appealing outcomes, all while ensuring computational efficiency [77]. Specifically, the perceptual loss is as follows:

$$\mathcal{L}_{per} = \frac{1}{3} \sum_{k=0}^2 \frac{1}{CHW} \|\phi(\hat{\mathbf{X}}_k) - \phi(\mathbf{I}_k)\|_1, \quad (7)$$

where C , H , and W denote the dimensions of the feature map obtained from the *Conv5.4* layer of the pre-trained VGGNet ϕ .

The final loss function \mathcal{L} to train our proposed GridFormer is shown as follows:

$$\mathcal{L} = \mathcal{L}_{char} + \alpha \mathcal{L}_{per}, \quad (8)$$

where \mathcal{L}_{char} denotes the Charbonnier loss, \mathcal{L}_{per} is the perceptual loss. α is a hyper-parameter that is used to balance these two losses. In our experiments, it is empirically set to 0.1.

3.4 Differences from Existing Methods

While HRNet [74], HRFormer [90], and RevCol [5] utilize a grid-like structure, they diverge from our GridFormer. First, GridFormer captures multi-scale features directly from the pixel level, in contrast to HRNet and HRFormer which perform multi-scale feature extraction at the feature layer level, and RevCol, which does not incorporate a multi-scale mechanism. Second, GridFormer integrates a new self-attention mechanism to enhance the fusion of multi-scale features more effectively. This approach sets it apart from HRNet, HRFormer, and RevCol, which do not employ compact self-attention in their feature fusion processes. Third, our network is intricately designed for image restoration under adverse weather conditions, striving to produce images of superior quality. Unlike HRNet, HRFormer, and RevCol, which are not specifically engineered for this challenge, our network architecture is uniquely suited to tackle the complexities inherent in this task.

4 Experiments and Analysis

We evaluate our GridFormer for several image restoration tasks in severe weather conditions, including (1) image dehazing, (2) image desnowing, (3) raindrop removal, (4) image deraining and dehazing, and (5) multi-weather restoration. Specifically, in this section, we first introduce datasets, the implementation details of our GridFormer, and the comparison methods. Then, we show the restoration results of our GridFormer and the comparison with the state-of-the-art methods. Finally, we conduct extensive ablation studies to verify the effectiveness of modules in our GridFormer.

4.1 Experimental Setup

We evaluate GridFormer on several image restoration tasks under severe weather conditions.

Datasets. For image dehazing, the first setting uses ITS [37] to train the model and test it on indoor SOTS [37]. Another setting is training and testing on Haze4K [48] covering both indoor and outdoor scenes. Desnowing is evaluated on Snow100K [49]. Rain-Drop [56] is used for raindrop removal, and Outdoor-Rain [40] is used for image deraining and dehazing. For multi-weather restoration, we train the model on a combination of images degraded in adverse weather conditions similar to [54]. Table 1 lists the datasets used for the different tasks. In the following, we introduce the dataset and experimental details for specific tasks for image restoration in adverse weather conditions.

Image dehazing. Following [46, 58, 68, 70], we conduct our experiments on RESIDE [37] and Haze4K [48] datasets. Specifically, for the RESIDE dataset, we adopt Indoor Training Set (ITS) to train the model and test the model on the indoor set of the SOTS dataset. ITS contains 13,990 indoor pair images and the indoor set of the SOTS dataset includes 500 indoor pair images. For the Haze4K dataset, we follow the previous work [85]. The Haze4K dataset contains 3,000 haze and haze-free image pairs for training and 1,000 for testing. The Haze4K dataset is more challenging, which considers both indoor and outdoor scenes.

Image desnowing. For this task, we use the popular Snow100K dataset [49] for training and evaluating the proposed method. Snow100K contains 50,000 training and 50,000 testing images. The testing set has three sub-sets *i.e.*, Snow100K-S/M/L, which refers to different snowflake sizes (light/mid/heavy). The Snow100K-S, Snow100K-M, and Snow100K-L have 16611, 16588, and 16801 image pairs, respectively. In our experiment, we keep the same setup of [54]. Specifically, we use the

Table 1 Dataset summary on five tasks of image restoration in adverse weather conditions.

Task	Dataset	#Train	#Test
Image Dehazing	ITS [37]	13,990	0
	SOTS-Indoor [37]	0	500
	Haze4K [48]	3,000	1,000
Image Desnowing	Snow100K [49]	50,000	0
	Snow100K-S [49]	0	16,611
	Snow100K-L [49]	0	16,801
Raindrop Removal	RainDrop [56]	861	0
	RainDrop-Test [56]	0	51
Image Deraining & Image Dehazing	Outdoor-Rain [40]	9,000	0
	Outdoor-Rain-Test [40]	0	750
Multi-weather Restoration	All-weather [35]	18,069	0
	Snow100K-S [49]	0	16,611
	Snow100K-L [49]	0	16,801
	RainDrop-Test [56]	0	51
	Outdoor-Rain-Test [40]	0	750

training set to train our model and evaluate the proposed method on Snow100K-S and Snow100K-L.

Raindrop removal. Consistent with previous works [56, 35, 71, 54], we adopt a representative RainDrop dataset [56] for raindrop removal. The RainDrop dataset includes 861 synthetic raindrop training images and 58 images for testing.

Image deraining and dehazing. For this task, we train our GridFormer with Outdoor-Rain dataset [40], which considers dense synthetic rain streaks and provides realistic scene views. Therefore, this dataset is designed to solve the problem of image deraining and dehazing. It consists of 9,000 images for training and 750 for testing.

Multi-weather restoration. Following the previous works [35, 71, 54], we use a mixed dataset called All-weather, in which the training set contains 18,069 images sampled from Snow100K [49], Raindrop [56], and Outdoor-Rain [40]. We use the Snow100k-S/L test sets to evaluate the model’s performance for the image desnowing task. In addition, we adopt the testing sets of the RainDrop dataset and Outdoor-Rain dataset to evaluate the model’s performance for the raindrop removal task and image deraining & dehazing task, respectively.

Implementation details. We implemented GridFormer in PyTorch, using the AdamW optimizer [51] with $\beta_1 = 0.9$ and $\beta_2 = 0.999$. The learning rate is set to 3×10^{-4} and decreased to 10^{-6} using the cosine annealing decay strategy [50]. For each task, we train the model with different iterations and patch sizes. At training time we use random horizontal and vertical flips for data augmentation. Following the setup in [80, 71, 70], we evaluate the performance by PSNR and SSIM calculated in RGB space for image dehazing, and on the Y channel for other tasks.

Comparison methods. The comparison methods for the image dehazing task are traditional method DCP [22], CNN-based methods DehazeNet [4], MSCNN [62], AOD-Net [36], GFN [62], GCANet [8],

Table 2 Dehazing results on SOTS-indoor and Haze4K. Bold and underlined fonts denote the best and second-best results, respectively.

Type	Method	SOTS-Indoor [37]		Haze4K [48]	
		PSNR \uparrow	SSIM \uparrow	PSNR \uparrow	SSIM \uparrow
Dehazing Task	DCP [22]	16.62	0.818	14.01	0.760
	DehazeNet [4]	19.82	0.821	19.12	0.840
	MSCNN [62]	19.84	0.833	14.01	0.510
	AOD-Net [36]	32.33	0.950	27.17	0.898
	GFN [62]	22.30	0.880	-	-
	GCANet [8]	30.23	0.980	-	-
	GridDehazeNet [46]	32.16	0.984	23.29	0.930
	MSBDN [14]	33.67	0.985	22.99	0.850
	PFDN [15]	32.68	0.976	-	-
	FFA-Net [58]	36.39	0.989	<u>26.96</u>	<u>0.950</u>
	AECR-Net [79]	37.17	0.990	-	-
	DehazeF-B [68]	37.84	0.994	-	-
	MAXIM-2S [70]	<u>38.11</u>	<u>0.991</u>	-	-
	GridFormer	42.34	0.994	33.27	0.986

Table 3 Desnowing results on Snow100K-S/L. Bold and underlined fonts denote best and second-best results, respectively.

Type	Method	Snow100K-S [49]		Snow100K-L [49]	
		PSNR \uparrow	SSIM \uparrow	PSNR \uparrow	SSIM \uparrow
Desnowing Task	SPANet [75]	29.92	0.8260	23.70	0.7930
	JSTASR [11]	31.40	0.9012	25.32	0.8076
	RESCAN [43]	31.51	0.9032	26.08	0.8108
	DesnowNet [49]	32.33	0.9500	27.17	0.8983
	DDMSNet [97]	34.34	0.9445	28.85	0.8772
	SnowDiff ₆₄ [54]	<u>36.59</u>	<u>0.9626</u>	<u>30.43</u>	<u>0.9145</u>
	SnowDiff ₁₂₈ [54]	36.09	0.9545	30.28	0.9000
GridFormer	38.89	0.9698	33.09	0.9340	
Multi-weather Restoration	All-in-One [41]	-	-	28.33	0.8820
	TransWeather [71]	32.51	0.9341	29.31	0.8879
	Restormer [91]	36.08	0.9591	30.28	0.9124
	WeatherDiff ₆₄ [54]	35.83	0.9566	30.09	0.9041
	WeatherDiff ₁₂₈ [54]	35.02	0.9516	29.58	0.8941
	GridFormer-S	<u>36.68</u>	<u>0.9602</u>	<u>30.78</u>	<u>0.9167</u>
GridFormer	37.46	0.9640	31.71	0.9231	

GridDehazeNet [46], MSBDN [14], PFDN [15], FFA-Net [58], and AECR-Net [79], and recent transformer-based methods DehazeF-B [68], and MAXIM-2S [70]. For the task of image desnowing, the comparison methods are SPANet [75], JSTASR [11], RESCAN [43], DesnowNet [49], DDMSNet [97], SnowDiff₆₄ [54], and SnowDiff₁₂₈ [54]. As for the raindrop removal task, the comparison methods are pix2pix [25], DuRN [47], RaindropAttn [61], AttentiveGAN [56], IDT [80], RainDropDiff₆₄ [54], and RainDropDiff₁₂₈ [54]. The comparison methods for the image deraining and dehazing task are CycleGAN [103], pix2pix [25], HRGAN [40], PCNet [30], MPR-Net [92], RainHazeDiff₆₄ [54], and RainHazeDiff₁₂₈ [54]. Finally, the comparison methods for the multi-weather restoration task are All-in-One [41], TransWeather [71], Restormer [91], WeatherDiff₆₄ [54], and WeatherDiff₁₂₈ [54].

4.2 Experimental Results

Dehazing results. We perform image dehazing on different datasets to evaluate the performance of Grid-

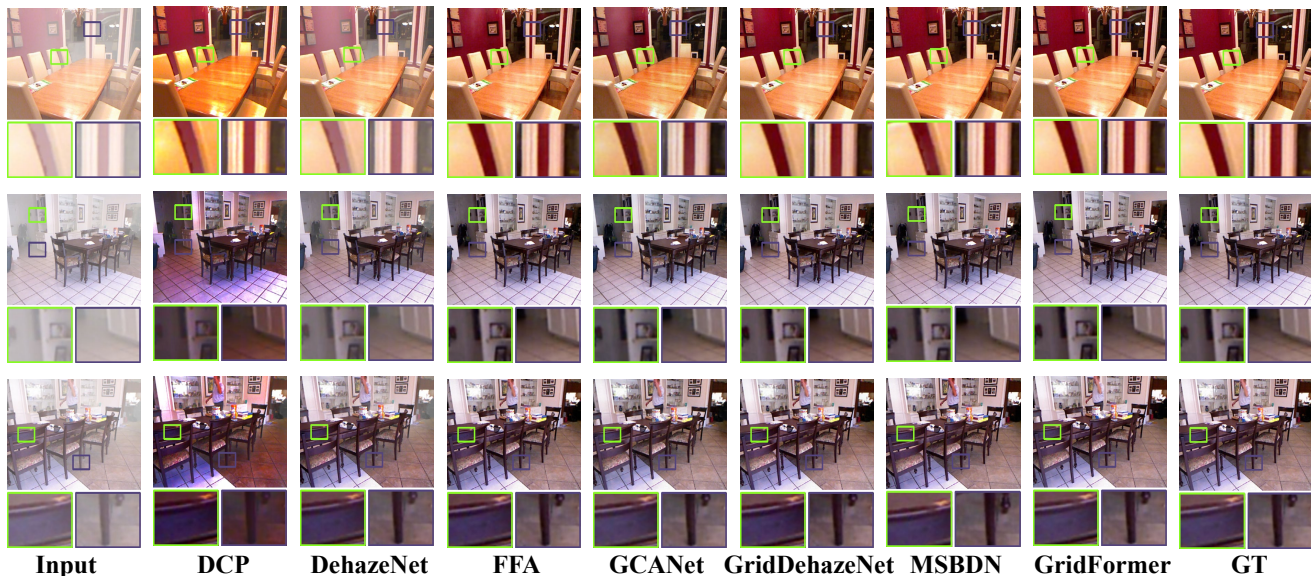


Fig. 6 Dehazing comparison on SOTS-indoor. From left to right are the input images, results of DCP [22], DehazeNet [4], FFA-Net [58], GCANet [8], GridDehazeNet [46], MSBDN [14], our GridFormer, and ground truth images, respectively. The images restored by GridFormer are more clear and closer to the ground truth. **Zoom in for details.**



Fig. 7 Desnowing comparison on Snow100K-S test set. From left to right are the input images, results of DesnowNet [49], DDMSNet [97], SnowDiff₆₄ [54], SnowDiff₁₂₈ [54], our GridFormer, and ground truth images, respectively. **Zoom in for details.**

Former. We compare the performance of GridFormer with various methods, including traditional prior-based methods, CNN-based methods, and recent transformer-based methods. Table 2 shows the quantitative results in terms of PSNR and SSIM. It shows that GridFormer achieves the best performance on the indoor subset of SOTS regarding all metrics. In particular, GridFormer

obtains a significant gain of 4.23 dB in PSNR compared to the second-best method MAXIM-2S [70].

We further compare the performance on the more challenging Haze4K dataset, which includes more realistic images from both indoor and outdoor scenarios. GridFormer obtains the best performance in terms of all metrics on this dataset as well. Fig. 6 provides a visual comparison for the SOTS indoor dataset. The

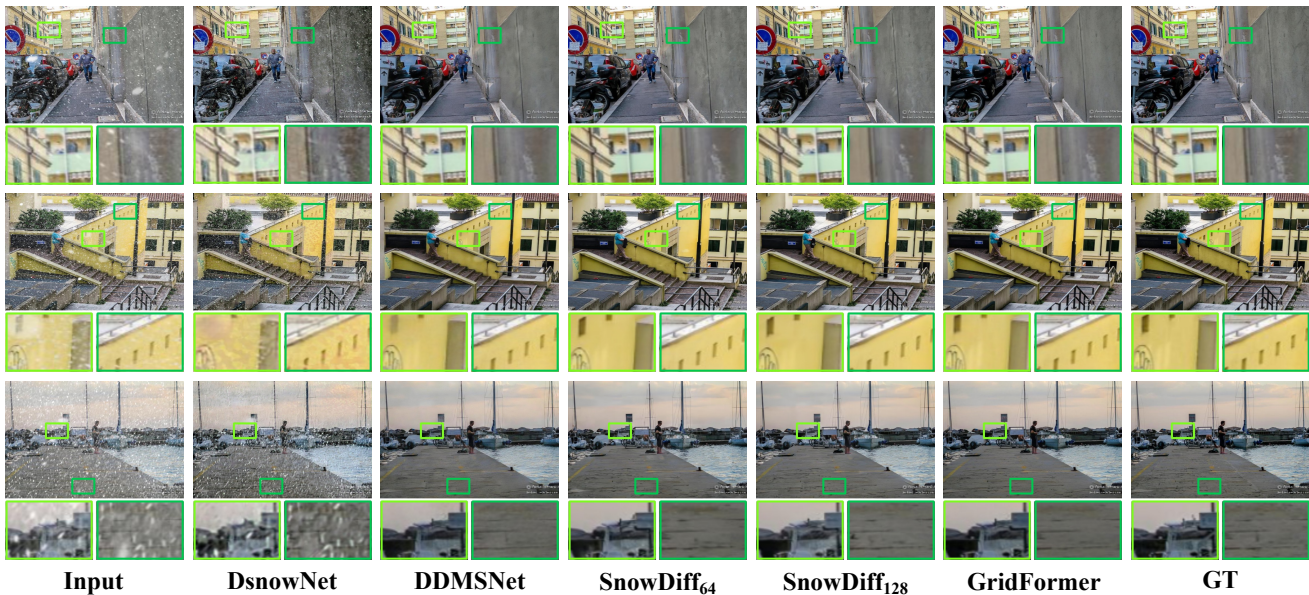


Fig. 8 Desnowing comparison on Snow100K-L test set. From left to right are the input images, results of DesnowNet [49], DDMSNet [97], SnowDiff₆₄ [54], SnowDiff₁₂₈ [54], our GridFormer, and ground truth images, respectively. **Zoom in for details.**

recovered images by GridFormer contain finer details and are closer to the ground truth.

Desnowing results. We evaluate the desnowing performance on the public Snow100K dataset [49]. The test set is divided into three subsets according to the particle size: Snow100K-S, Snow100K-M, and Snow100K-L. We select Snow100K-S and Snow100K-L for testing. Table 3 shows the quantitative results. On the Snow100K-S subset, GridFormer outperforms the diffusion-based method SnowDiff₆₄ [54] by 2.3 dB and by 0.0072 in terms of PSNR and SSIM. As for the most difficult Snow100K-L subset, GridFormer still gains an improvement of 2.66 dB and 0.0195 in terms of PSNR and SSIM compared to the second-best method SnowDiff₆₄. Fig. 7 and Fig. 8 provide the visual comparisons, showing that GridFormer is effective in removing image corruption due to snow while producing perceptually pleasing results.

RainDrop removal results. In Table 4 we present the quantitative results for raindrop removal on the RainDrop dataset. For an extensive comparison, we compare GridFormer with seven different methods: pix2pix [25], DuRN [47], RaindropAttn [61], AttentiveGAN [56], IDT [80], RainDropDiff₆₄ [54], and RainDropDiff₁₂₈ [54]. The results show that GridFormer is competitive. Specifically, GridFormer achieves the best performance in terms of PSNR and achieves almost the same level of performance as the state-of-the-art method RainDropDiff₆₄ [54] in terms of SSIM with a difference of 0.0022. A visual comparison

Table 4 RainDrop removal results on RainDrop test set. Bold and underlined fonts denote best and second-best results, respectively.

Type	Method	RainDrop [56]	
		PSNR \uparrow	SSIM \uparrow
RainDrop Removal	pix2pix [25]	28.02	0.8547
	DuRN [47]	31.24	0.9259
	RaindropAttn [61]	31.44	0.9263
	AttentiveGAN [56]	31.59	0.9170
	IDT [80]	31.87	0.9313
	RainDropDiff ₆₄ [54]	32.29	0.9422
	RainDropDiff ₁₂₈ [54]	32.43	0.9334
	GridFormer	32.92	<u>0.9400</u>
Multi-weather Restoration	All-in-One [41]	<u>31.12</u>	0.9268
	TransWeather [71]	30.17	0.9157
	Restormer [91]	30.91	0.9282
	WeatherDiff ₆₄ [54]	29.64	<u>0.9312</u>
	WeatherDiff ₁₂₈ [54]	29.66	0.9225
	GridFormer-S	31.02	0.9301
	GridFormer	32.39	0.9362

of the results on RainDrop is provided in Fig. 9. It shows that our method can remove raindrops successfully and generate realistic images.

Deraining and dehazing results. For the image deraining and dehazing task, we conduct experiments on the Outdoor-Rain dataset [40]. This dataset has 9,000 pairs of images for training, and 750 pairs for testing, where degraded images are synthesized considering the rain and haze scenes simultaneously. The comparisons between GridFormer and other state-of-the-art methods are reported in Table 5. GridFormer outperforms other competitors in terms of PSNR, and ranks second place regarding SSIM. More specifically, GridFormer achieves 0.11 dB and 0.46 dB improvement in



Fig. 9 Raindrop removal results on RainDrop test set. From left to right are the input images, results of RainDropAttn [61], AttentiveGAN [56], RainDropDiff₆₄ [54], RainDropDiff₁₂₈ [54], our GridFormer, and ground truth images, respectively. **Zoom in for details.**



Fig. 10 Visual results of deraining & dehazing on Outdoor-Rain test set. From left to right are the input images, results of HRGAN [40], MPRNet [92], RainHazeDiff₆₄ [54], RainHazeDiff₁₂₈ [54], our GridFormer, and ground truth images, respectively. **Zoom in for details.**

terms of PSNR when compared to RainHazeDiff₆₄ [54] and MPRNet [92]. Fig. 10 shows the visual comparison, indicating that GridFormer can handle haze and rain-fall scenarios well at the same time, and generate vivid results.

Multi-weather restoration results. We further explore the potential of GridFormer for multi-weather restoration. Specifically, we first train our model on

the mixed dataset sampled from Snow100K [49], Raindrop [56], and Outdoor-Rain [40] datasets. Then, we evaluate our model on the Snow100k-S/L test sets, the RainDrop test dataset, and the Outdoor-Rain test dataset. We choose four representative multi-weather restoration methods for comparison: All-in-One network [41] is a CNN-based method, TransWeather is based on transformers, WeatherDiff₆₄

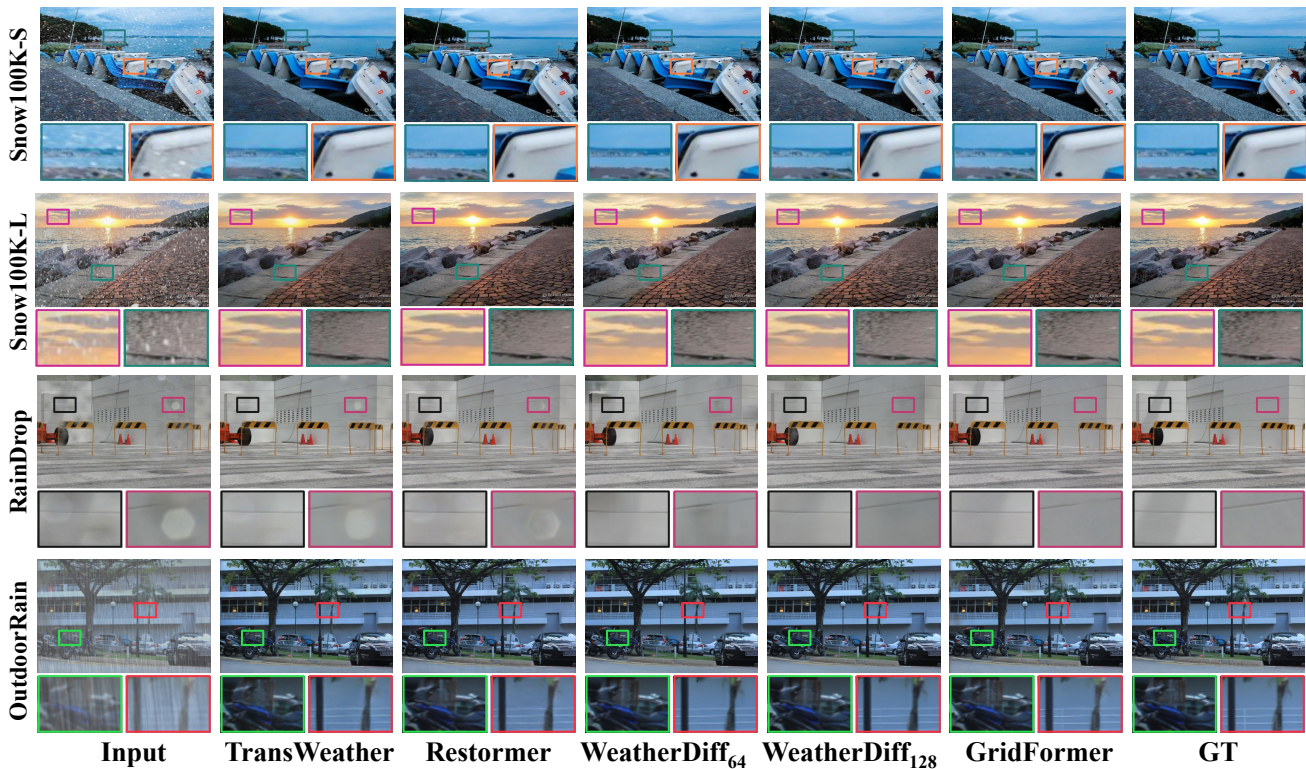


Fig. 11 Multi-weather Restoration comparison on Snow100K-S, Snow100K-L, RainDrop, Outdoor-Rain datasets. From left to right are the input images, results of TransWeather [71], Restormer [91], WeatherDiff₆₄ [54], WeatherDiff₁₂₈ [54], our GridFormer, and ground truth images, respectively. **Zoom in for details.**

Table 5 Image deraining & dehazing results on Outdoor-Rain test set. The MACs of each model is measured on 256 × 256 image.

Type	Method	Outdoor-Rain [40] PSNR↑	SSIM↑	Overhead Param/MACs
Deraining & Dehazing	CycleGAN [103]	17.62	0.6560	7.84M/42.38G
	pix2pix [25]	19.09	0.7100	54.41M/18.15G
	HRGAN [40]	21.56	0.8550	25.11M/34.93G
	PCNet [30]	26.19	0.9015	627.56K/268.45G
	MPRNet [92]	28.03	0.9192	3.64M/148.55G
	RainHazeDiff ₆₄ [54]	<u>28.38</u>	0.9320	82.92M/475.16G
	RainHazeDiff ₁₂₈ [54]	26.84	0.9152	85.56M/263.45G
	GridFormer	28.49	<u>0.9213</u>	30.12M/251.35G
Multi-weather Restoration	All-in-One [41]	24.71	0.8980	44.00M/12.26G
	TransWeather [71]	28.83	0.9000	21.90M/5.64G
	Restormer [91]	30.21	0.9208	26.10M/140.99G
	WeatherDiff ₆₄ [54]	29.64	0.9312	82.92M/475.16G
	WeatherDiff ₁₂₈ [54]	29.72	0.9216	85.56M/263.45G
	GridFormer-S	<u>30.48</u>	<u>0.9313</u>	14.83M/133.24G
	GridFormer	31.87	0.9335	30.12M/251.35G

and WeatherDiff₁₂₈ are diffusion models. Table 3, 4, and 5 summarize the quantitative results. GridFormer achieves the best performance in all weather conditions. We present visual comparisons in Fig. 11. Images produced by GridFormer exhibit fewer artifacts and are closer to ground truth compared to other methods. In an additional experiment, we set $C = 32$ in the grid head to construct a tiny variant of the network called GridFormer-S for comparison. The results show that

Table 6 Cross-dataset evaluation. Models are trained only on the All-weather dataset and directly applied to the Rain100L and Test100 benchmark datasets. Bold and underlined fonts denote the best and second-best results, respectively.

Method	Rain100L [83]		Test100 [96]	
	PSNR↑	SSIM↑	PSNR↑	SSIM↑
TransWeather	30.33	0.9365	24.20	0.8317
Restormer	27.08	0.8432	23.28	0.7136
WeatherDiff ₆₄	27.46	0.8534	23.13	0.7091
WeatherDiff ₁₂₈	27.56	0.8552	23.26	0.7255
GridFormer-S	<u>33.21</u>	<u>0.9541</u>	<u>27.10</u>	<u>0.8713</u>
GridFormer	34.24	0.9649	29.26	0.8912

our methods achieve competitive results with less complexity and parameters, see Table 5.

Cross-dataset evaluation. To further verify the models’ performance across different datasets, we conduct a cross-dataset evaluation on different SOTA methods. To be specific, the models (*i.e.*, TransWeather, Restormer, WeatherDiff₆₄, WeatherDiff₁₂₈, GridFormer-S, and GridFormer) are trained on the All-weather dataset, and then directly applied to the specific deraining datasets Rain100L [83] and Test100 [96] for testing. Experimental results in Table 6 show that our GridFormer-S and GridFormer outperform other approaches.

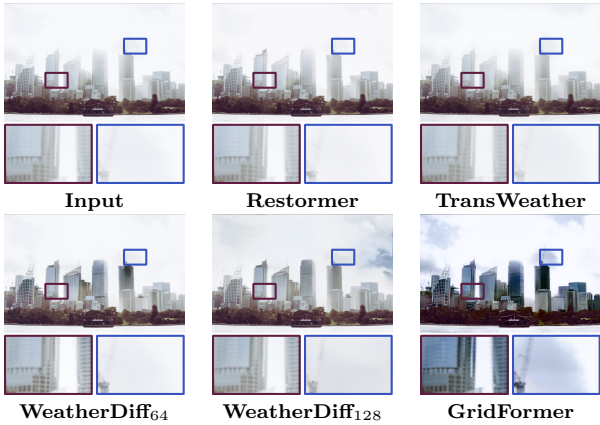


Fig. 12 Exemplar results on the real-world image.

Table 7 Memory consumption and inference time of different methods evaluated on 512×512 resolution images.

Methods	Platform	Memory (MB)	time (ms)
Restormer	PyTorch	30031.50	321.6
WeatherDiff ₆₄	PyTorch	6307.53	101232.1
WeatherDiff ₁₂₈	PyTorch	7941.03	133557.7
GridFormer-S	PyTorch	20793.94	165.0
GridFormer	PyTorch	28461.94	259.1

Performance in real-world scenarios. To further verify the effectiveness of the proposed method in real-world scenarios, we conduct a qualitative comparison experiment on the real-world hazy image from the Internet. The comparison result is shown in Fig. 12. Compared with current state-of-the-art methods, our method effectively removes the haze and produces a clear result. The result shows that our method outperforms the current methods in real-world scenarios.

Efficiency comparison. We also analyze the efficiency of our models. Table 7 displays the comparison results of different methods in terms of the memory consumption and inference time for 512×512 resolution. Specifically, we choose top three SOTA methods (*i.e.*, Restormer, WeatherDiff₆₄, and WeatherDiff₁₂₈) for comparison. Compared with other SOTA methods, our GridFormer-S exhibits the highest inference time. In addition, GridFormer-S and GridFormer are competitive in terms of memory consumption.

4.3 Application

Image restoration in adverse weather conditions can enhance the image content, which can be easily incorporated into other high-level vision tasks. As a result, we investigate the potential of GridFormer in improving the performance of object detection, image segmentation, and image caption algorithms when dealing with adverse weather scenes. In the case of object detec-

Table 8 Ablation studies on the proposed compact-enhanced self-attention (CESA). FS, CS, and LE refer to feature sampling, channel split, and local enhancement operations in CESA respectively. MACs are measured on 256×256 images.

FS	CS	LE	Param/MACs	RainDrop	SOTS-Indoor
				PSNR/SSIM	PSNR/SSIM
✗	✗	✗	38.08M/322.26G	29.93/0.8710	36.89/0.9631
✓	✗	✗	34.91M/237.79G	30.82/0.9012	37.81/0.9831
✓	✓	✗	26.88M/227.65G	31.98/0.9294	40.51/0.9921
✓	✓	✓	30.12M/251.35G	32.57/0.9365	41.84/0.9932

tion, we consider both synthetic and real-world images. Fig. 13 shows detection results, where we use Google Vision API for object detection. We observe that haze, rain, and snow greatly reduce the detection accuracy, that is, increased missed detection, higher false detection, and lower detection confidence. In contrast, the detection accuracy and confidence of the images recovered by GridFormer show significant improvement over those of weather-degraded images. Fig. 14 showcases the segmentation results, utilizing the state-of-the-art Segment Anything Model [33] for image segmentation. Our restoration results demonstrate an enhancement in segmentation accuracies, indicating that GridFormer effectively facilitates subsequent segmentation performance. Lastly, Fig. 15 presents the image caption results using the BLIP model [38]. These results show that the BLIP model can generate detailed captions by utilizing our restoration results, further validating the effectiveness of our GridFormer.

4.4 Ablation Study

We conduct extensive ablation studies to verify the proposed compact-enhanced self-attention, residual dense transformer block, grid structure, and used loss functions. Specifically, we conduct ablation studies on the tasks of raindrop removal and dehazing to analyze the performance of GridFormer. For each model, we train it for 2×10^5 iterations using a batch size of 12 on the RainDrop dataset [56] and the ITS dataset [37] respectively. Subsequently, we assess the performance of each model on the testing sets of the RainDrop dataset and the testing SOTS-Indoor dataset. The detailed results are presented as follows.

A. Compact-enhanced self-attention. We verify the impact of feature sampling, channel split, and local enhancement operations in compact-enhanced self-attention. Table 8 shows the comparison results. After applying feature sampling (FS) and channel split (CS) operations respectively, the model achieves 0.89 dB and 1.16 dB improvements in the RainDrop dataset (0.92

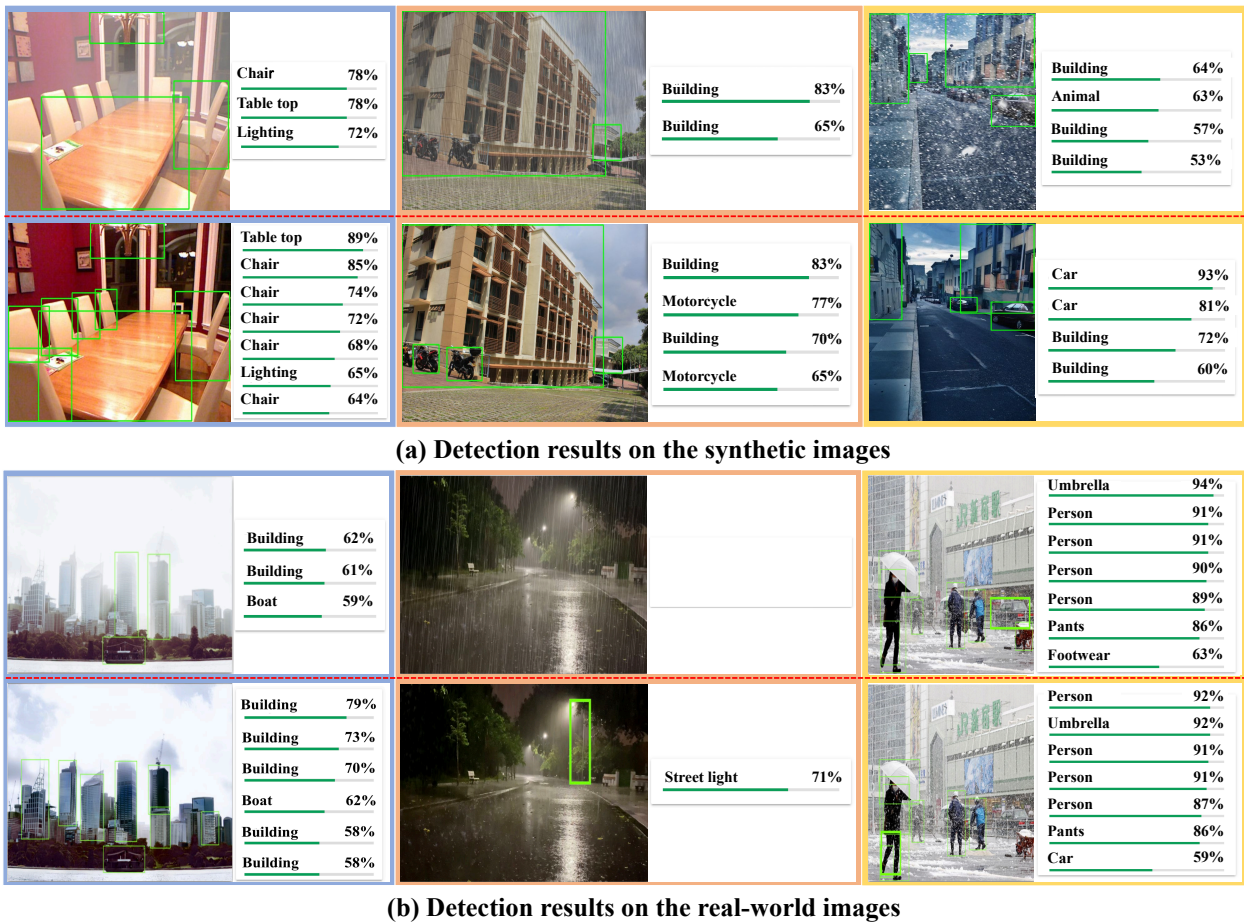


Fig. 13 In each sub-image, the top images are captured in haze, rain, and snow weather conditions. The bottom images are recovered by our GridFormer. We report the detection confidences of these images, which shows that our GridFormer as a pre-processing tool benefits the task of object detection.

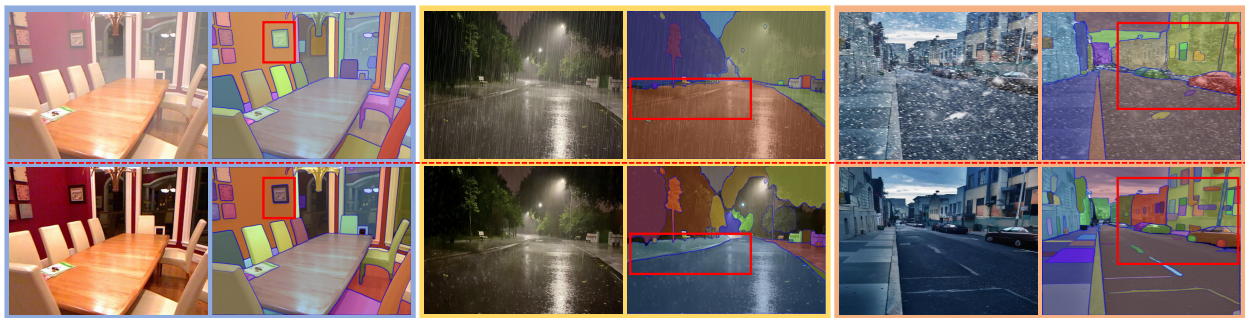


Fig. 14 The top images are captured in haze, rain, and snow weather conditions. The bottom images are recovered by our GridFormer. We show the segmentation results of these images, which demonstrates that our GridFormer as a pre-processing tool benefits the task of image segmentation.

dB and 2.70 dB improvements in the SOTS-Indoor dataset), while the computational complexity is significantly reduced. Using local enhancement (LE) operations, the performance gains on the RainDrop and SOTS-Indoor datasets are 0.59 dB and 1.33 dB respectively. The ablation study results suggest the effectiveness of these operations. We also conduct an additional

ablation study on the RainDrop dataset to verify the effectiveness of exchanging the Values for feature interaction and fusion in our compact-enhanced self-attention. Specifically, we focus on exchanging only the Queries between \mathbf{z}_1 and \mathbf{z}_2 to investigate its impact on performance. The results of this experiment demonstrate that exchanging the Queries results in a PSNR value



Fig. 15 In each sub-image, the top images are captured in haze, rain, and snow weather conditions. The bottom images are recovered by our GridFormer. We show the image caption results of these images, which shows that our GridFormer as a pre-processing tool benefits the task of image caption.

Table 9 Ablation studies on the different settings of r in three rows of GridFormer layers, where r indicates the stride of the average pooling operation in feature sampling of the proposed compact-enhanced transformer layer. [4, 2, 2] denotes r is set as 4, 2, and 2 in three rows of GridFormer layers, respectively.

Different Settings of r	Param/MACs	RainDrop	SOTS-Indoor
		PSNR/SSIM	PSNR/SSIM
[2, 2, 2]	29.53M/213.01G	30.93/0.8991	33.81/0.9631
[4, 4, 4]	48.63M/356.57G	31.62/0.9112	40.31/0.9901
[4, 2, 2]	30.12M/251.35G	31.98/0.9294	40.51/0.9921

Table 10 Ablation studies on the proposed residual dense transformer block (RDTB). DC, LF, and LSC denote dense connection, local fusion with 1×1 convolution, and local skip connection in RDTB respectively. MACs are measured on 256×256 images.

DC	LF	LSC	Param/MACs	RainDrop	SOTS-Indoor
				PSNR/SSIM	PSNR/SSIM
\times	\times	\times	27.99M/253.57G	31.48/0.9187	40.32/0.9901
\checkmark	\times	\times	32.78M/284.87G	32.07/0.9284	40.45/0.9912
\checkmark	\checkmark	\times	30.12M/251.35G	32.05/0.9298	40.87/0.9926
\checkmark	\checkmark	\checkmark	30.12M/251.35G	32.57/0.9365	41.84/0.9932

of 31.81, which is inferior to the outcome achieved by exchanging the Values (32.57). These ablation results show the effectiveness of the Value exchange in enhancing interaction and feature fusion, thereby contributing to improved restoration performance. Furthermore, in our model, the choice of the step parameter r , as described in formula 3, indeed impacts the model’s computational complexity and performance. Thus, we evaluate the effect of different settings of r in the GridFormer. Table 9 shows that our model with the [4, 2, 2] setting achieves a better trade-off between computation cost and performance.

B. Residual dense transformer block. To demonstrate the effectiveness of the proposed residual dense transformer block, we conduct ablation studies by considering the following three factors: (1) dense connections (DC), (2) local fusion with 1×1 convolution

Table 11 Ablation study on different grid configurations. r and c denote the numbers of rows and columns of the model.

Grid Setting		Overhead		RainDrop	SOTS-Indoor
r	c	Param (M)	MACs (G)	PSNR/SSIM	PSNR/SSIM
$r = 1$	$c = 3$	0.81	51.24	30.07/0.9163	38.02/0.9879
	$c = 4$	1.01	64.01	30.44/0.9198	38.21/0.9880
	$c = 5$	1.21	76.77	30.54/0.9199	38.61/0.9885
	$c = 6$	1.41	89.54	30.62/0.9205	38.78/0.9891
$r = 2$	$c = 3$	2.64	80.48	31.21/0.9280	39.68/0.9900
	$c = 4$	3.50	103.98	31.23/0.9281	39.73/0.9901
	$c = 5$	4.51	129.52	31.37/0.9294	40.21/0.9915
	$c = 6$	5.37	153.01	31.58/0.9311	40.50/0.9918
$r = 3$	$c = 3$	13.96	125.38	31.67/0.9339	40.79/0.9918
	$c = 4$	19.09	166.01	31.73/0.9356	41.13/0.9929
	$c = 5$	24.99	210.72	31.89/0.9359	41.01/0.9926
	$c = 6$	30.12	251.35	32.57/0.9365	41.84/0.9932
$r = 4$	$c = 6$	150.86	410.09	32.05/0.9361	40.85/0.9921

(LF), and (3) local skip connection (LSC). Specifically, we analyze the different models by progressively adding these components. The results are shown in Table 10. We observe that each component improves the performance, where dense connections contribute the most.

C. Exploring different configurations in the grid structure of GridFormer. To comprehensively understand the impact of GridFormer’s grid structure, we have conducted ablation experiments involving variations in the number of rows and columns. Each row within our GridFormer framework corresponds to a distinct scale, while the columns in the grid fusion module act as conduits that facilitate the exchange of information across diverse scales. This grid structure profoundly influences the information interchange that occurs among the grid units within the Grid Fusion module. In our study, we have systematically altered the number of rows, ranging from 1 to 4, while maintaining columns at values of 3, 4, 5, and 6. The results with different configurations are shown in Table 11. By increasing r and c , the performance is improved, and the overhead gradually becomes complex. The model performance achieves its maximum for $r = 3$ and $c = 6$. Thus, we select these values in our final model.

D. Other GridFormer components. The skip connection from input images and the perceptual loss

also contribute to improving the performance. Without the skip connection from the input image, the PSNR value would decrease from 32.57 dB to 31.85 dB on the testing set of the RainDrop dataset. Training GridFormer without the perceptual loss results in a PSNR of 32.72 dB on the testing set of the RainDrop dataset.

5 Limitations and Future Work

As a new backbone, GridFormer has achieved better performance than previous methods in image restoration under adverse weather conditions, but it still has space for improvement. For example, using the pre-trained strategy [9] or the contrastive learning technique [79] on our GridFormer can further explore its performance potential. In addition, we fuse multi-scale features with simple weighted attention [102, 76]. We can improve this fusion by designing special modules using sophisticated attention mechanisms [58, 68]. Finally, GridFormer is evaluated in the image scenery, and we are still exploring whether it can handle the video restoration problem. In the future, it is also an important direction to extend our GridFormer to deal with video restoration in adverse weather conditions.

6 Conclusion

In this paper, we propose GridFormer, a unified Transformer architecture for image restoration in adverse weather conditions. It adopts a grid structure to facilitate information communication across different streams and makes full use of the hierarchical features from the input images. In addition, to build the basic layer of GridFormer, we propose a compact-enhanced transformer layer and integrate it in a residual dense manner, which encourages feature reuse and enhances feature representation. Comprehensive experiments show that GridFormer significantly surpasses state-of-the-art methods, producing good results on both weather-specific and multi-weather restoration tasks.

Acknowledgement

This work was supported in part by the National Natural Science Foundation of China (GrantNo. 62372223, 62372480), in part by the Guangdong Basic and Applied Basic Research Foundation (No. 2023A1515012839), in part by Shenzhen Science and Technology Program (No. JSGG20220831093004008), in part by China Mobile Zijin Innovation Institute (No. NR2310J7M).

Data Availability Statement

The datasets generated during and/or analyzed during the current study are available in the WeatherDiffusion repository, with the link as <https://github.com/IGITUGraz/WeatherDiffusion>.

References

1. Ali, A.M., Benjdira, B., Koubaa, A., El-Shafai, W., Khan, Z., Boulila, W.: Vision transformers in image restoration: A survey. *Sensors* **23**(5), 2385 (2023) [7](#)
2. Ba, Y., Zhang, H., Yang, E., Suzuki, A., Pfahnl, A., Chandrappa, C.C., de Melo, C.M., You, S., Soatto, S., Wong, A., et al.: Not just streaks: Towards ground truth for single image deraining. In: *Proceedings of European Conference on Computer Vision*, pp. 723–740 (2022) [3](#)
3. Berman, D., Avidan, S., et al.: Non-local image dehazing. In: *Proceedings of IEEE Conference on Computer Vision and Pattern Recognition*, pp. 1674–1682 (2016) [3](#)
4. Cai, B., Xu, X., Jia, K., Qing, C., Tao, D.: Dehazenet: An end-to-end system for single image haze removal. *IEEE Transactions on Image Processing* **25**(11), 5187–5198 (2016) [1, 3, 9, 10](#)
5. Cai, Y., Zhou, Y., Han, Q., Sun, J., Kong, X., Li, J., Zhang, X.: Reversible column networks. In: *Proceedings of International Conference on Learning Representations* (2022) [2, 8](#)
6. Carion, N., Massa, F., Synnaeve, G., Usunier, N., Kirillov, A., Zagoruyko, S.: End-to-end object detection with transformers. In: *Proceedings of European Conference on Computer Vision*, pp. 213–229 (2020) [1](#)
7. Charbonnier, P., Blanc-Feraud, L., Aubert, G., Barlaud, M.: Two deterministic half-quadratic regularization algorithms for computed imaging. In: *Proceedings of International Conference on Image Processing*, pp. 168–172 (1994) [5, 7](#)
8. Chen, D., He, M., Fan, Q., Liao, J., Zhang, L., Hou, D., Yuan, L., Hua, G.: Gated context aggregation network for image dehazing and deraining. In: *Proceedings of IEEE Winter Conference on Applications of Computer Vision*, pp. 1375–1383 (2019) [9, 10](#)
9. Chen, H., Wang, Y., Guo, T., Xu, C., Deng, Y., Liu, Z., Ma, S., Xu, C., Xu, C., Gao, W.: Pre-trained image processing transformer. In: *Proceedings of IEEE Conference on Computer Vision and Pattern Recognition*, pp. 12299–12310 (2021) [4, 17](#)
10. Chen, S., Ye, T., Liu, Y., Chen, E., Shi, J., Zhou, J.: Snowformer: Scale-aware transformer via context interaction for single image desnowing. *arXiv preprint arXiv:2208.09703* (2022) [3](#)
11. Chen, W.T., Fang, H.Y., Ding, J.J., Tsai, C.C., Kuo, S.Y.: Jstasr: Joint size and transparency-aware snow removal algorithm based on modified partial convolution and veiling effect removal. In: *Proceedings of European Conference on Computer Vision*, pp. 754–770 (2020) [3, 9](#)
12. Chen, Y.L., Hsu, C.T.: A generalized low-rank appearance model for spatio-temporally correlated rain streaks. In: *Proceedings of IEEE International Conference on Computer Vision*, pp. 1968–1975 (2013) [1](#)

13. Cho, S.J., Ji, S.W., Hong, J.P., Jung, S.W., Ko, S.J.: Re-thinking coarse-to-fine approach in single image deblurring. In: Proceedings of the IEEE International Conference on Computer Vision, pp. 4641–4650 (2021) [4](#)
14. Dong, H., Pan, J., Xiang, L., Hu, Z., Zhang, X., Wang, F., Yang, M.H.: Multi-scale boosted dehazing network with dense feature fusion. In: Proceedings of IEEE Conference on Computer Vision and Pattern Recognition, pp. 2157–2167 (2020) [2](#), [3](#), [9](#), [10](#)
15. Dong, J., Pan, J.: Physics-based feature dehazing networks. In: Proceedings of European Conference on Computer Vision, pp. 188–204 (2020) [9](#)
16. Dosovitskiy, A., Beyer, L., Kolesnikov, A., Weissenborn, D., Zhai, X., Unterthiner, T., Dehghani, M., Minderer, M., Heigold, G., Gelly, S., et al.: An image is worth 16x16 words: Transformers for image recognition at scale. In: Proceedings of International Conference on Learning Representations (2021) [6](#)
17. Du, Y., Xu, J., Zhen, X., Cheng, M.M., Shao, L.: Conditional variational image deraining. *IEEE Transactions on Image Processing* **29**, 6288–6301 (2020) [3](#)
18. Fu, X., Huang, J., Ding, X., Liao, Y., Paisley, J.: Clearing the skies: A deep network architecture for single-image rain removal. *IEEE Transactions on Image Processing* **26**(6), 2944–2956 (2017) [1](#), [3](#)
19. Garg, K., Nayar, S.K.: When does a camera see rain? In: Proceedings of IEEE International Conference on Computer Vision, pp. 1067–1074 (2005) [1](#)
20. Glorot, X., Bordes, A., Bengio, Y.: Deep sparse rectifier neural networks. In: Proceedings of International Conference on Artificial Intelligence and Statistics, pp. 315–323 (2011) [6](#)
21. Gu, X., Wang, L., Deng, Z., Cao, Y., Huang, X., Zhu, Y.m.: Adafuse: Adaptive medical image fusion based on spatial-frequency cross attention. *arXiv preprint arXiv:2310.05462* (2023) [7](#)
22. He, K., Sun, J., Tang, X.: Single image haze removal using dark channel prior. *IEEE Transactions on Pattern Analysis and Machine Intelligence* **33**(12), 2341–2353 (2010) [1](#), [3](#), [9](#), [10](#)
23. Hsu, W.Y., Chang, W.C.: Wavelet approximation-aware residual network for single image deraining. *IEEE Transactions on Pattern Analysis and Machine Intelligence* (2023) [7](#)
24. Huang, G., Liu, Z., Van Der Maaten, L., Weinberger, K.Q.: Densely connected convolutional networks. In: Proceedings of IEEE Conference on Computer Vision and Pattern Recognition, pp. 4700–4708 (2017) [6](#)
25. Isola, P., Zhu, J.Y., Zhou, T., Efros, A.A.: Image-to-image translation with conditional adversarial networks. In: Proceedings of IEEE Conference on Computer Vision and Pattern Recognition, pp. 1125–1134 (2017) [9](#), [11](#), [13](#)
26. Itti, L., Koch, C., Niebur, E.: A model of saliency-based visual attention for rapid scene analysis. *IEEE Transactions on Pattern Analysis and Machine Intelligence* **20**(11), 1254–1259 (1998) [1](#)
27. Jaw, D.W., Huang, S.C., Kuo, S.Y.: Desnowgan: An efficient single image snow removal framework using cross-resolution lateral connection and gans. *IEEE Transactions on Circuits and Systems for Video Technology* **31**(4), 1342–1350 (2020) [2](#)
28. Jiang, K., Wang, Z., Yi, P., Chen, C., Han, Z., Lu, T., Huang, B., Jiang, J.: Decomposition makes better rain removal: An improved attention-guided deraining network. *IEEE Transactions on Circuits and Systems for Video Technology* **31**(10), 3981–3995 (2020) [7](#)
29. Jiang, K., Wang, Z., Yi, P., Chen, C., Huang, B., Luo, Y., Ma, J., Jiang, J.: Multi-scale progressive fusion network for single image deraining. In: Proceedings of IEEE Conference on Computer Vision and Pattern Recognition, pp. 8346–8355 (2020) [2](#)
30. Jiang, K., Wang, Z., Yi, P., Chen, C., Wang, Z., Wang, X., Jiang, J., Lin, C.W.: Rain-free and residue hand-in-hand: A progressive coupled network for real-time image deraining. *IEEE Transactions on Image Processing* **30**, 7404–7418 (2021) [9](#), [13](#)
31. Johnson, J., Alahi, A., Fei-Fei, L.: Perceptual losses for real-time style transfer and super-resolution. In: Proceedings of European Conference on Computer Vision, pp. 694–711 (2016) [5](#)
32. Kang, L.W., Lin, C.W., Fu, Y.H.: Automatic single-image-based rain streaks removal via image decomposition. *IEEE Transactions on Image Processing* **21**(4), 1742–1755 (2011) [3](#)
33. Kirillov, A., Mintun, E., Ravi, N., Mao, H., Rolland, C., Gustafson, L., Xiao, T., Whitehead, S., Berg, A.C., Lo, W.Y., et al.: Segment anything. *arXiv preprint arXiv:2304.02643* (2023) [14](#)
34. Lee, H., Choi, H., Sohn, K., Min, D.: Knn local attention for image restoration. In: Proceedings of IEEE Conference on Computer Vision and Pattern Recognition, pp. 2139–2149 (2022) [7](#)
35. Li, B., Liu, X., Hu, P., Wu, Z., Lv, J., Peng, X.: All-in-one image restoration for unknown corruption. In: Proceedings of IEEE Conference on Computer Vision and Pattern Recognition, pp. 17452–17462 (2022) [2](#), [3](#), [9](#)
36. Li, B., Peng, X., Wang, Z., Xu, J., Feng, D.: Aodnet: All-in-one dehazing network. In: Proceedings of IEEE International Conference on Computer Vision, pp. 4770–4778 (2017) [3](#), [9](#)
37. Li, B., Ren, W., Fu, D., Tao, D., Feng, D., Zeng, W., Wang, Z.: Benchmarking single-image dehazing and beyond. *IEEE Transactions on Image Processing* **28**(1), 492–505 (2018) [2](#), [8](#), [9](#), [14](#)
38. Li, J., Li, D., Xiong, C., Hoi, S.: Blip: Bootstrapping language-image pre-training for unified vision-language understanding and generation. In: Proceedings of International Conference on Machine Learning, pp. 12888–12900 (2022) [14](#)
39. Li, P., Yun, M., Tian, J., Tang, Y., Wang, G., Wu, C.: Stacked dense networks for single-image snow removal. *Neurocomputing* **367**, 152–163 (2019) [1](#), [3](#)
40. Li, R., Cheong, L.F., Tan, R.T.: Heavy rain image restoration: Integrating physics model and conditional adversarial learning. In: Proceedings of IEEE Conference on Computer Vision and Pattern Recognition, pp. 1633–1642 (2019) [2](#), [3](#), [8](#), [9](#), [11](#), [12](#), [13](#)
41. Li, R., Tan, R.T., Cheong, L.F.: All in one bad weather removal using architectural search. In: Proceedings of IEEE Conference on Computer Vision and Pattern Recognition, pp. 3175–3185 (2020) [2](#), [3](#), [9](#), [11](#), [12](#), [13](#)
42. Li, X., Hua, Z., Li, J.: Two-stage single image dehazing network using swin-transformer. *IET Image Processing* **16**(9), 2518–2534 (2022) [7](#)
43. Li, X., Wu, J., Lin, Z., Liu, H., Zha, H.: Recurrent squeeze-and-excitation context aggregation net for single image deraining. In: Proceedings of European Conference on Computer Vision, pp. 254–269 (2018) [3](#), [9](#)
44. Liang, J., Cao, J., Sun, G., Zhang, K., Van Gool, L., Timofte, R.: Swinir: Image restoration using swin transformer. In: Proceedings of IEEE International Conference on Computer Vision, pp. 1833–1844 (2021) [4](#)

45. Liang, Y., Anwar, S., Liu, Y.: Drt: A lightweight single image deraining recursive transformer. In: Proceedings of IEEE Conference on Computer Vision and Pattern Recognition, pp. 589–598 (2022) [4](#)
46. Liu, X., Ma, Y., Shi, Z., Chen, J.: Griddehazenet: Attention-based multi-scale network for image dehazing. In: Proceedings of IEEE International Conference on Computer Vision, pp. 7314–7323 (2019) [2](#), [3](#), [6](#), [8](#), [9](#), [10](#)
47. Liu, X., Suganuma, M., Sun, Z., Okatani, T.: Dual residual networks leveraging the potential of paired operations for image restoration. In: Proceedings of IEEE Conference on Computer Vision and Pattern Recognition, pp. 7007–7016 (2019) [2](#), [3](#), [9](#), [11](#)
48. Liu, Y., Zhu, L., Pei, S., Fu, H., Qin, J., Zhang, Q., Wan, L., Feng, W.: From synthetic to real: Image dehazing collaborating with unlabeled real data. In: Proceedings of ACM International Conference on Multimedia, pp. 50–58 (2021) [2](#), [8](#), [9](#)
49. Liu, Y.F., Jaw, D.W., Huang, S.C., Hwang, J.N.: Desnownet: Context-aware deep network for snow removal. *IEEE Transactions on Image Processing* **27**(6), 3064–3073 (2018) [1](#), [2](#), [3](#), [8](#), [9](#), [10](#), [11](#), [12](#)
50. Loshchilov, I., Hutter, F.: Sgdr: Stochastic gradient descent with warm restarts. *arXiv preprint arXiv:1608.03983* (2016) [9](#)
51. Loshchilov, I., Hutter, F.: Decoupled weight decay regularization. In: Proceedings of International Conference on Learning Representations (2019) [9](#)
52. Luo, Y., Xu, Y., Ji, H.: Removing rain from a single image via discriminative sparse coding. In: Proceedings of IEEE International Conference on Computer Vision, pp. 3397–3405 (2015) [3](#)
53. Narasimhan, S.G., Nayar, S.K.: Chromatic framework for vision in bad weather. In: Proceedings of IEEE Conference on Computer Vision and Pattern Recognition, pp. 598–605 (2000) [3](#)
54. Özdenizci, O., Legenstein, R.: Restoring vision in adverse weather conditions with patch-based denoising diffusion models. *IEEE Transactions on Pattern Analysis and Machine Intelligence* (2023) [2](#), [3](#), [8](#), [9](#), [10](#), [11](#), [12](#), [13](#)
55. Petit, O., Thome, N., Rambour, C., Themyr, L., Collins, T., Soler, L.: U-net transformer: Self and cross attention for medical image segmentation. In: Proceedings of Machine Learning in Medical Imaging, pp. 267–276 (2021) [7](#)
56. Qian, R., Tan, R.T., Yang, W., Su, J., Liu, J.: Attentive generative adversarial network for raindrop removal from a single image. In: Proceedings of IEEE Conference on Computer Vision and Pattern Recognition, pp. 2482–2491 (2018) [2](#), [3](#), [8](#), [9](#), [11](#), [12](#), [14](#)
57. Qiao, Y., Huo, Z., Meng, S.: Dual-route synthetic-to-real adaption for single image dehazing. *IET Image Processing* (2023) [7](#)
58. Qin, X., Wang, Z., Bai, Y., Xie, X., Jia, H.: Ffa-net: Feature fusion attention network for single image dehazing. In: Proceedings of AAAI Conference on Artificial Intelligence, pp. 11908–11915 (2020) [3](#), [8](#), [9](#), [10](#), [17](#)
59. Qu, Y., Chen, Y., Huang, J., Xie, Y.: Enhanced pix2pix dehazing network. In: Proceedings of IEEE Conference on Computer Vision and Pattern Recognition, pp. 8160–8168 (2019) [2](#), [3](#)
60. Quan, R., Yu, X., Liang, Y., Yang, Y.: Removing raindrops and rain streaks in one go. In: Proceedings of IEEE Conference on Computer Vision and Pattern Recognition, pp. 9147–9156 (2021) [3](#)
61. Quan, Y., Deng, S., Chen, Y., Ji, H.: Deep learning for seeing through window with raindrops. In: Proceedings of IEEE International Conference on Computer Vision, pp. 2463–2471 (2019) [3](#), [9](#), [11](#), [12](#)
62. Ren, W., Liu, S., Zhang, H., Pan, J., Cao, X., Yang, M.H.: Single image dehazing via multi-scale convolutional neural networks. In: Proceedings of European Conference on Computer Vision, pp. 154–169 (2016) [1](#), [3](#), [9](#)
63. Ren, W., Ma, L., Zhang, J., Pan, J., Cao, X., Liu, W., Yang, M.H.: Gated fusion network for single image dehazing. In: Proceedings of IEEE Conference on Computer Vision and Pattern Recognition, pp. 3253–3261 (2018) [3](#)
64. Ren, W., Tian, J., Han, Z., Chan, A., Tang, Y.: Video desnowing and deraining based on matrix decomposition. In: Proceedings of IEEE Conference on Computer Vision and Pattern Recognition, pp. 4210–4219 (2017) [3](#)
65. Roth, S., Black, M.J.: Fields of experts: A framework for learning image priors. In: Proceedings of IEEE Conference on Computer Vision and Pattern Recognition, vol. 2, pp. 860–867 (2005) [1](#)
66. Shi, W., Caballero, J., Huszár, F., Totz, J., Aitken, A.P., Bishop, R., Rueckert, D., Wang, Z.: Real-time single image and video super-resolution using an efficient sub-pixel convolutional neural network. In: Proceedings of IEEE Conference on Computer Vision and Pattern Recognition, pp. 1874–1883 (2016) [5](#)
67. Simonyan, K., Zisserman, A.: Very deep convolutional networks for large-scale image recognition. *arXiv preprint arXiv:1409.1556* (2014) [8](#)
68. Song, Y., He, Z., Qian, H., Du, X.: Vision transformers for single image dehazing. *arXiv preprint arXiv:2204.03883* (2022) [3](#), [8](#), [9](#), [17](#)
69. Susladkar, O., Deshmukh, G., Makwana, D., Mittal, S., Teja, R., Singhal, R.: Gafnet: A global fourier self attention based novel network for multi-modal downstream tasks. In: Proceedings of the IEEE Winter Conference on Applications of Computer Vision, pp. 5242–5251 (2023) [7](#)
70. Tu, Z., Talebi, H., Zhang, H., Yang, F., Milanfar, P., Bovik, A., Li, Y.: Maxim: Multi-axis mlp for image processing. In: Proceedings of IEEE Conference on Computer Vision and Pattern Recognition, pp. 5769–5780 (2022) [4](#), [8](#), [9](#), [10](#)
71. Valanarasu, J.M.J., Yasarla, R., Patel, V.M.: Transweather: Transformer-based restoration of images degraded by adverse weather conditions. In: Proceedings of IEEE Conference on Computer Vision and Pattern Recognition, pp. 2353–2363 (2022) [2](#), [3](#), [7](#), [9](#), [11](#), [13](#)
72. Vaswani, A., Shazeer, N., Parmar, N., Uszkoreit, J., Jones, L., Gomez, A.N., Kaiser, L., Polosukhin, I.: Attention is all you need. In: Proceedings of Advances in Neural Information Processing Systems (2017) [4](#), [6](#)
73. Wang, H., Xie, Q., Zhao, Q., Meng, D.: A model-driven deep neural network for single image rain removal. In: Proceedings of IEEE Conference on Computer Vision and Pattern Recognition, pp. 3103–3112 (2020) [3](#)
74. Wang, J., Sun, K., Cheng, T., Jiang, B., Deng, C., Zhao, Y., Liu, D., Mu, Y., Tan, M., Wang, X., et al.: Deep high-resolution representation learning for visual recognition. *IEEE Transactions on Pattern Analysis and Machine Intelligence* **43**(10), 3349–3364 (2020) [2](#), [8](#)
75. Wang, T., Yang, X., Xu, K., Chen, S., Zhang, Q., Lau, R.W.: Spatial attentive single-image deraining with a high quality real rain dataset. In: Proceedings of IEEE

- Conference on Computer Vision and Pattern Recognition, pp. 12270–12279 (2019) [1](#), [3](#), [9](#)
76. Wang, T., Zhang, K., Shen, T., Luo, W., Stenger, B., Lu, T.: Ultra-high-definition low-light image enhancement: A benchmark and transformer-based method. In: Proceedings of AAAI Conference on Artificial Intelligence (2023) [5](#), [17](#)
 77. Wang, X., Yu, K., Wu, S., Gu, J., Liu, Y., Dong, C., Qiao, Y., Change Loy, C.: Esrgan: Enhanced super-resolution generative adversarial networks. In: Proceedings of the European Conference on Computer Vision Workshops (2018) [7](#), [8](#)
 78. Wang, Z., Cun, X., Bao, J., Zhou, W., Liu, J., Li, H.: Uformer: A general u-shaped transformer for image restoration. In: Proceedings of IEEE Conference on Computer Vision and Pattern Recognition, pp. 17683–17693 (2022) [4](#), [7](#)
 79. Wu, H., Qu, Y., Lin, S., Zhou, J., Qiao, R., Zhang, Z., Xie, Y., Ma, L.: Contrastive learning for compact single image dehazing. In: Proceedings of IEEE Conference on Computer Vision and Pattern Recognition, pp. 10551–10560 (2021) [9](#), [17](#)
 80. Xiao, J., Fu, X., Liu, A., Wu, F., Zha, Z.J.: Image de-raining transformer. *IEEE Transactions on Pattern Analysis and Machine Intelligence* (2022) [3](#), [9](#), [11](#)
 81. Yamashita, A., Tanaka, Y., Kaneko, T.: Removal of adherent waterdrops from images acquired with stereo camera. In: Proceedings of International Conference on Intelligent Robots and Systems, pp. 400–405 (2005) [3](#)
 82. Yang, W., Tan, R.T., Feng, J., Guo, Z., Yan, S., Liu, J.: Joint rain detection and removal from a single image with contextualized deep networks. *IEEE Transactions on Pattern Analysis and Machine Intelligence* **42**(6), 1377–1393 (2019) [3](#)
 83. Yang, W., Tan, R.T., Feng, J., Liu, J., Guo, Z., Yan, S.: Deep joint rain detection and removal from a single image. In: Proceedings of the IEEE Conference on Computer Vision and Pattern Recognition, pp. 1357–1366 (2017) [13](#)
 84. Yao, C., Jin, S., Liu, M., Ban, X.: Dense residual transformer for image denoising. *Electronics* **11**(3), 418 (2022) [4](#)
 85. Ye, T., Jiang, M., Zhang, Y., Chen, L., Chen, E., Chen, P., Lu, Z.: Perceiving and modeling density is all you need for image dehazing. In: Proceedings of European Conference on Computer Vision (2021) [8](#)
 86. Ye, T., Zhang, Y., Jiang, M., Chen, L., Liu, Y., Chen, S., Chen, E.: Perceiving and modeling density for image dehazing. In: Proceedings of European Conference on Computer Vision, pp. 130–145 (2022) [7](#)
 87. Yin, X., Tu, G., Chen, Q.: Multiscale depth fusion with contextual hybrid enhancement network for image dehazing. *IEEE Transactions on Instrumentation and Measurement* (2023) [7](#)
 88. You, S., Tan, R.T., Kawakami, R., Mukaigawa, Y., Ikeuchi, K.: Adherent raindrop modeling, detection and removal in video. *IEEE Transactions on Pattern Analysis and Machine Intelligence* **38**(9), 1721–1733 (2015) [1](#), [3](#)
 89. Yu, H., Zheng, N., Zhou, M., Huang, J., Xiao, Z., Zhao, F.: Frequency and spatial dual guidance for image dehazing. In: Proceedings of European Conference on Computer Vision, pp. 181–198 (2022) [7](#)
 90. Yuan, Y., Fu, R., Huang, L., Lin, W., Zhang, C., Chen, X., Wang, J.: Hrformer: High-resolution vision transformer for dense predict. In: Proceedings of Advances in Neural Information Processing Systems, pp. 7281–7293 (2021) [2](#), [8](#)
 91. Zamir, S.W., Arora, A., Khan, S., Hayat, M., Khan, F.S., Yang, M.H.: Restormer: Efficient transformer for high-resolution image restoration. In: Proceedings of IEEE Conference on Computer Vision and Pattern Recognition, pp. 5728–5739 (2022) [4](#), [9](#), [11](#), [13](#)
 92. Zamir, S.W., Arora, A., Khan, S., Hayat, M., Khan, F.S., Yang, M.H., Shao, L.: Multi-stage progressive image restoration. In: Proceedings of IEEE Conference on Computer Vision and Pattern Recognition, pp. 14821–14831 (2021) [2](#), [4](#), [9](#), [12](#), [13](#)
 93. Zhang, F., Chen, G., Wang, H., Zhang, C.: Cf-dan: Facial-expression recognition based on cross-fusion dual-attention network. *Computational Visual Media* pp. 1–16 (2024) [7](#)
 94. Zhang, H., Patel, V.M.: Densely connected pyramid dehazing network. In: Proceedings of IEEE Conference on Computer Vision and Pattern Recognition, pp. 3194–3203 (2018) [1](#), [3](#)
 95. Zhang, H., Patel, V.M.: Density-aware single image de-raining using a multi-stream dense network. In: Proceedings of IEEE Conference on Computer Vision and Pattern Recognition, pp. 695–704 (2018) [3](#)
 96. Zhang, H., Sindagi, V., Patel, V.M.: Image de-raining using a conditional generative adversarial network. *IEEE Transactions on Circuits and Systems for Video Technology* **30**(11), 3943–3956 (2019) [3](#), [13](#)
 97. Zhang, K., Li, R., Yu, Y., Luo, W., Li, C.: Deep dense multi-scale network for snow removal using semantic and depth priors. *IEEE Transactions on Image Processing* **30**, 7419–7431 (2021) [1](#), [2](#), [3](#), [6](#), [9](#), [10](#), [11](#)
 98. Zhang, T., Jiang, N., Lin, J., Lin, J., Zhao, T.: Desnowformer: an effective transformer-based image desnowing network. In: Proceedings of IEEE International Conference on Visual Communications and Image Processing, pp. 1–5 (2022) [3](#)
 99. Zhang, X., Wang, T., Wang, J., Tang, G., Zhao, L.: Pyramid channel-based feature attention network for image dehazing. *Computer Vision and Image Understanding* **197**, 103003 (2020) [2](#), [3](#)
 100. Zhang, Y., Tian, Y., Kong, Y., Zhong, B., Fu, Y.: Residual dense network for image super-resolution. In: Proceedings of IEEE Conference on Computer Vision and Pattern Recognition, pp. 2472–2481 (2018) [6](#)
 101. Zhang, Z., Zhu, Y., Fu, X., Xiong, Z., Zha, Z.J., Wu, F.: Multifocal attention-based cross-scale network for image de-raining. In: Proceedings of the 29th ACM International Conference on Multimedia, pp. 3673–3681 (2021) [3](#)
 102. Zheng, L., Li, Y., Zhang, K., Luo, W.: T-net: Deep stacked scale-iteration network for image dehazing. *IEEE Transactions on Multimedia* (2022) [5](#), [6](#), [17](#)
 103. Zhu, J.Y., Park, T., Isola, P., Efros, A.A.: Unpaired image-to-image translation using cycle-consistent adversarial networks. In: Proceedings of IEEE International Conference on Computer Vision, pp. 2223–2232 (2017) [9](#), [13](#)
 104. Zhu, L., Fu, C.W., Lischinski, D., Heng, P.A.: Joint bi-layer optimization for single-image rain streak removal. In: Proceedings of IEEE International Conference on Computer Vision, pp. 2526–2534 (2017) [3](#)